

Article

Seamless Modeling of Direct and Indirect Aerosol Effects during April 2020 Wildfire Episode in Ukraine

Mykhailo Savenets ^{1,*}, Valeriia Rybchynska ^{1,2}, Alexander Mahura ³, Roman Nuterman ⁴,
Alexander Baklanov ^{4,5}, Markku Kulmala ³ and Tuukka Petäjä ^{3,*}

- ¹ Ukrainian Hydrometeorological Institute, 03028 Kyiv, Ukraine; valeriia.rybchynska@studio.unibo.it
² Department of Physics and Astronomy, University of Bologna, 40126 Bologna, Italy
³ Institute for Atmospheric and Earth System Research, University of Helsinki, 00014 Helsinki, Finland; alexander.mahura@helsinki.fi (A.M.); markku.kulmala@helsinki.fi (M.K.)
⁴ Niels Bohr Institute, University of Copenhagen, 2100 Copenhagen, Denmark; nuterman@nbi.ku.dk (R.N.); abaklanov@wmo.int (A.B.)
⁵ World Meteorological Organization, CH-1211 Geneva, Switzerland
* Correspondence: savenets@uhmi.org.ua (M.S.); tuukka.petaja@helsinki.fi (T.P.)

Abstract: Wildfires frequently occur in Ukraine during agricultural open-burning seasons in spring and autumn. High aerosol concentrations from fire emissions can significantly affect meteorological processes via direct and indirect aerosol effects. To study these impacts, we selected a severe wildfire episode from April 2020 in the Chernobyl Exclusion Zone (CEZ) and its surrounding area as a case study. We employed the Enviro-HIRLAM modeling system to simulate reference (REF) meteorological conditions, along with direct (DAE), indirect (IDAE), and combined (COMB) aerosol effects. In our simulations, black carbon (BC) and organic carbon (OC) comprised 70–80% of all aerosol mass in the region, represented in two layers of higher concentrations: one near the surface and the other 3–4 km above the surface. Our simulations showed that the inclusion of aerosol effects into the modeling framework led to colder (up to -3 °C) and drier (relative humidity drop up to -20%) conditions near the surface. We also observed localized changes in cloudiness, precipitation (mainly redistribution), and wind speed (up to ± 4 m/s), particularly during the movement of atmospheric cold fronts. Larger uncertainties were observed in coarser model simulations when direct aerosol effects were considered. Quantifying the aerosol effects is crucial for predicting and promptly detecting changes that could exacerbate unfavorable weather conditions and wildfires. Such knowledge is essential for improving the effectiveness of emergency response measures.

Keywords: Chernobyl Exclusion Zone; forest fires; black carbon; organic carbon; Enviro-HIRLAM



Citation: Savenets, M.; Rybchynska, V.; Mahura, A.; Nuterman, R.; Baklanov, A.; Kulmala, M.; Petäjä, T. Seamless Modeling of Direct and Indirect Aerosol Effects during April 2020 Wildfire Episode in Ukraine. *Atmosphere* **2024**, *15*, 550. <https://doi.org/10.3390/atmos15050550>

Academic Editor: Griša Močnik

Received: 8 March 2024

Revised: 19 April 2024

Accepted: 26 April 2024

Published: 29 April 2024



Copyright: © 2024 by the authors. Licensee MDPI, Basel, Switzerland. This article is an open access article distributed under the terms and conditions of the Creative Commons Attribution (CC BY) license (<https://creativecommons.org/licenses/by/4.0/>).

1. Introduction

Wildfires are a major natural source of aerosols, affecting both air quality [1] and atmospheric processes [2]. Globally, large areas are burned every year, with a concerning trend towards increased wildfire frequency due to climate change [3,4]. This problem is particularly relevant for Ukraine, where the wildfire frequency is rising [5], exacerbated by the negative impact of the Russia–Ukraine war [6,7]. Among the most dangerous were wildfires in the Chernobyl Exclusion Zone (CEZ) that occur in the abandoned radioactively contaminated areas. In April 2020, a few sporadic fires turned into one of the most devastating wildfire episodes in Ukraine and raised concern among scientists because of the possible environmental consequences, e.g., air quality impacts [8], emission of radioactive materials [9], and atmospheric transport and dispersion of radionuclides [10].

Aerosols induce climatological and meteorological changes at the global [11,12], regional [13,14], and local [15] scales through direct and indirect aerosol effects [16]. Including aerosol effects in numerical weather prediction (NWP) models can notably enhance weather and air quality forecasts [17]. Previous studies have reported that biomass burning aerosols

generally lead to the cooling of the near-surface layer [18–20]; a reduction in sensible heat fluxes [18,21]; and varied impacts on rain and hail formation [22,23], cloudiness [24], and humidity [15,20,21]. The interactions of the aerosols with radiative processes and cloud microphysics can, to a certain extent, induce changes in atmospheric circulation [25,26].

Despite the advancements in weather models that include aerosol effects, numerous uncertainties remain. Many of them arise from non-optimal representation of aerosols in the modeling framework and challenges in the parameterizations of aerosol-related processes in cloud microphysics and cloud dynamics [27]. Some reported aerosol effects have different influences on meteorological variables, e.g., on precipitation [28]. For example, White et al. (2017) [29] reported on the increasing role of aerosol effects in models and proper microphysical parameterizations. Addressing these uncertainties requires studies focused on specific climate regimes [27].

Considering the increasing frequency of wildfires in Ukraine due to open burning, this study aims to explore how the distributions of meteorological parameters are modulated during wildfires by both direct and indirect aerosol effects. Section 2 provides a description of the model used in this study, the Environment–High-Resolution Limited Area Model (Enviro-HIRLAM), as well as summarizes the details about the study period, the geographical area of interest, and the process of model verification using meteorological observations. Model validation with the spatio-temporal distribution of aerosols will be discussed in Section 3. Subsequently, the impact of aerosol direct and indirect forcing on meteorological parameters will be evaluated and discussed in Section 4, followed by the conclusions in Section 5.

2. Materials and Methods

2.1. Study Area

During the studied period, severe wildfires occurred in the CEZ and the neighboring territories of the Zhytomyr region of Ukraine (see Figure 1). The overall period was divided into two sub-periods with different locations of wildfire spots. The wildfires were mostly distributed in the CEZ before 14 April 2020, and after this date, the fires were concentrated in the north of the Zhytomyr region. The prevailing synoptic weather patterns transported the wildfire emissions to the south, south-west, and west, affecting Ukrainian territory. Therefore, the study area was set as the entire Ukraine, with a focus on the northern and central parts. We selected 18 synoptic stations for the validation of the model results as follows: 14 stations are located in the city centers of administrative regions (oblasts) in Ukraine, and 4 stations are in Belarus, north from the CEZ area. Note that 6 out of 18 synoptic stations were outside the 2 km resolution model domain (or fall into its halo-zone), and therefore, their data were not included in the analysis for this domain.



Figure 1. Studied area and boundaries of model domains with locations and names of selected synoptic stations and areas of interest.

This study spans the month of April 2020, specifically concentrating on the timeframe from 4 April to 21 April 2020. This interval was marked by intense wildfires in Ukraine's northern regions, encompassing the CEZ. For modeling purposes and our analysis, we employed the Enviro-HIRLAM, which is a fully online-integrated modeling system [30].

2.2. Enviro-HIRLAM Model Description and Design of the Experiments

Model simulations were initially performed at a horizontal resolution of 15 km, followed by downscaled model runs to 5 km and 2 km resolutions. The selection of boundaries for these modeling domains considered the locations of the wildfires and the patterns of atmospheric circulation. Specifically, the domain with a 2 km resolution, comprising 310×310 grid points, encompassed the areas affected by the wildfires, the CEZ, and the Kyiv metropolitan region, which allow future research on aerosol impacts in urban area. The 5 km domain includes the entire territory of Ukraine with 310×310 grid points, while the 15 km domain, consisting of 190×240 grid points, covered a broader European area, enabling the investigation of prevalent western and north-western atmospheric transport towards Ukraine.

The timestep for the Enviro-HIRLAM simulations was set at 240 s for 15 km, 120 s for 5 km, and 60 s for 2 km horizontal resolution. The model output was saved at 3 h intervals. The vertical model grid included 40 hybrid levels. Four different model regimes were used in the Enviro-HIRLAM simulations. A reference run (REF) was carried out without the direct and indirect aerosol effects, which is a normal procedure in NWP models. Three other model runs were carried out including the direct aerosol effects (DAEs), indirect aerosol effects (IDAEs), and combined effects of both (COMB). These simulations allowed us to quantify the impact of aerosols on the spatio-temporal distribution of meteorological parameters.

The necessary input data for our study included both natural and anthropogenic emissions, as well as spatial data for meteorological and chemical parameters. We utilized a variety of emission inventories, including IS4FIRES (<https://is4fires.fmi.fi>, accessed on 20 April 2024) and IASA's ECLIPSEv5 (Evaluating the Climate and Air Quality Impacts of Short-Lived Pollutants for specific sectors identified by Selected Nomenclature for Air Pollution (SNAP) codes). The initial and boundary conditions as 3-hourly meteorological 3D fields were extracted from the ERA5 model archives at the European Centre for Medium-Range Weather Forecasts (ECMWF). The sea surface temperature at 12 h intervals and meteorological observations at 3 h intervals in Binary Universal Form for the Representation (BUFR) format were assimilated into the modeling framework. The initial and boundary conditions also included 3D fields of aerosols and gaseous components at 3 h intervals derived from the Copernicus Atmosphere Monitoring Service (CAMS) of the ECMWF.

The computations were performed using the resources of the Puhti supercomputer system provided by the Center for Science Computing (CSC) HPC (Finland). The configuration of each model run included 7 compute nodes; 40 MPI tasks per node (in total, 280 cores), with 17 MPI sub-domains along longitude and 15 MPI subdomains along latitude; and 12 points for the boundary zone (4 passive boundary points and 8 halo-zone points).

2.3. Meteorological Observations

The model results were compared with the observation data from 18 synoptic stations distributed at different distances from the wildfires (see Figure 1). We used five basic meteorological parameters for verification: 2 m air temperature ($^{\circ}\text{C}$), 2 m relative humidity (%), 10 m wind speed (m/s), total cloud cover (units from 0 to 10 were converted to fractions), and 6 h accumulated precipitation (mm). Then, 10 m wind speed and direction were calculated from the horizontal (u,v) components of wind in the Enviro-HIRLAM output.

In order to compare the precipitation data with the synoptic stations, the model's 3 h output was recalculated into 6 h accumulated precipitation at 00, 06, 12, and 18 UTC (Universal Coordinated Time).

Unfortunately, there are almost no observations of aerosol concentrations at the Ukrainian air quality network, which had already been discussed in [8,31]. Only total suspended coarse particle concentrations were available, but without size or chemical classification. Hence, we were not able to include any verification of modeled aerosol component information regarding different modeled aerosol components (black carbon, organic carbon, dust, or sulfates) in this study.

2.4. Tools for Model Verification

Model verification for the meteorological parameters mentioned in Section 2.3 was performed for all model runs (REF, DAE, IDAE, and COMB) and all spatial resolutions (15, 5, and 2 km), being compared to meteorological observations at synoptic stations. To show the agreement between modeled and observed data, we used the Pearson correlation coefficient. It was calculated based on the 6 h time series of accumulated precipitation and the 3 h time series for the rest of the parameters. Each variable used for correlation contained 3456 elements for 15 km horizontal resolution, 3328 elements for 5 km, and 2000 elements for 2 km. The number of elements in the variables of accumulated precipitation was smaller because of the 6 h temporal resolution and being considered only for the hours when precipitation was observed and/or present in the simulations. Hence, each variable of precipitation contained 751 elements for 15 km horizontal resolution, 565 elements for 5 km, and 430 elements for 2 km.

We used five statistical metrics (errors) to estimate model runs against meteorological observations: mean bias (mean error, ME), mean absolute error (MAE), mean squared error (MSE), root-mean-square error (RMSE), and mean absolute percentage error (MAPE) [32].

2.5. Overview of the Synoptic Situation

Relatively dry weather conditions during March–early April 2020 prevailed before the wildfires. This initiated the seasonal burning of agricultural fields and plant residues in private gardens and yards. Numerous open-burning hotspots were started and went out of control. They turned into large wildfires in the north of Ukraine, as shown in Figure 1.

In the beginning of April, area with wildfires increased, and they started to influence the air quality of nearby cities. The wildfires were distributed to the CEZ. During that time, weather conditions over the northern part of Ukraine were influenced by a deep cyclone (mean sea-level pressure (MSLP) about 970 hPa) with a center over Scandinavia (Figure A1). At this time, the MSLP in Ukraine was relatively high and varied from 1008 to 1015 hPa. Within a week, the cyclone moved north while a high-pressure system (MSLP of about 1025 hPa) developed over western Europe. This synoptic development influenced the weather in Ukraine and resulted in a multidirectional wind variation over the geographical region of the wildfires. On 10 April 2020, the warm weather front (see Figure A2) caused a north-western wind, which significantly affected air quality in the Kyiv metropolitan area.

The anticyclone over western Europe developed and covered larger areas until 14 April 2020, influencing the western part of Ukraine, where MSLP reached 1020 hPa. At the same time, a lengthy atmospheric occlusion (originating from the low-pressure system in northern Europe) and a stationary front passed through Ukraine, bringing precipitation (see Figure 2). Because of this stationary front over Ukraine, the study period can be conditionally divided into two shorter periods. The first period (4–14 April 2020) ended after the front passed Ukraine because the majority of wildfires in the CEZ were extinguished by precipitation. However, the subsequent weather changes with strong winds favored the dispersion of new wildfires and a dust storm event. This second period of intense wildfires covered 15–23 April 2020.

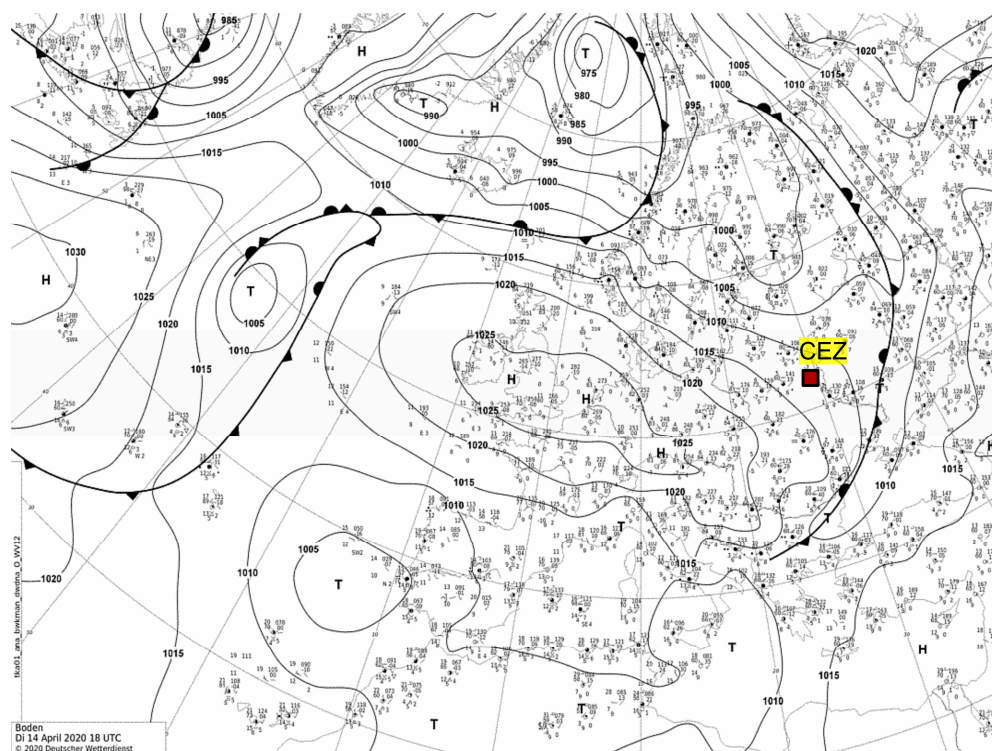


Figure 2. German Weather Service (DWD) archive synoptic map at 18 UTC on 14 April 2020 (source https://www.wetter3.de/archiv_dwd_dt.html; accessed on 13 October 2023), with the red square corresponding to the CEZ location.

During 15–16 April 2020, the pressure difference between a low-pressure system in northern Europe (with a MSLP of about 980 hPa) and a high-pressure system over the Black Sea (with a MSLP of about 1025 hPa) resulted in strong western–northwestern winds over Ukraine (see Figure A3). It caused the formation of the dust storm event on 16 April 2020 that deteriorated air quality in Ukraine, in particular, over its northern part. As it was discussed in [8], the dust storm passed a distance of 400 km in a matter of 6–7 h, reaching the Kyiv metropolitan area. On 17 April 2020, the cold weather front passed over Ukraine (see Figure A4). Strong winds enhanced the transport of the pollution plume from the wildfire areas into a large area, clearly visible for more than 800 km away from the point of origin based on remote sensing data [8].

After 18 April 2020, the wildfires were gradually extinguished. The synoptic situation was favorable for limiting and stopping fire distribution due to the low-gradient pressure field and wind speed decrease. At the end of the wildfire episodes, the MSLP over Ukraine varied from 1015 to 1020 hPa (see Figure A5).

3. Results

3.1. Verification of Modeled vs. Observed Meteorology

We performed a verification of the Enviro-HIRLAM model results against available meteorological observations to understand whether aerosols during the wildfire episode had influenced the distribution of meteorological parameters. Verification of the REF simulations against the observations showed the accuracy of numerical modeling, and evaluation of the DAE, IDAE, and COMB model simulation results against the observations allowed for the identification of the impacts of relevant aerosol effects capable of influencing weather conditions. If the simulations with DAE, IDAE, or COMB effects showed a better correspondence to the meteorological observations than the REF case, then the inclusion of the aerosol effects significantly improved the representation of the meteorological parameters.

The correlation coefficients between the observed meteorological data and the model output for REF, DAE, IDAE, and COMB runs of the model at the 15, 5 and 2 km spatial resolutions are summarized in Table 1. In general, higher and better correlations were found for the 2 m air temperature and the 2 m relative humidity. Lower coefficient values were found for the 10 m wind speed, and the lowest ones were found for the total cloud cover and the accumulated precipitation.

Table 1. Correlation between model results and observed meteorological data.

Horizontal Resolution	Model Mode			
	REF	DAE	IDAE	COMB
2 m air temperature				
15 km	0.96	0.89	0.96	0.89
5 km	0.96	0.94	0.96	0.94
2 km	0.96	0.95	0.96	0.95
2 m relative humidity				
15 km	0.86	0.81	0.86	0.81
5 km	0.85	0.83	0.86	0.84
2 km	0.83	0.83	0.84	0.83
10 m wind speed				
15 km	0.77	0.68	0.77	0.67
5 km	0.76	0.74	0.76	0.74
2 km	0.77	0.80	0.82	0.80
Total cloud cover				
15 km	0.60	0.52	0.61	0.51
5 km	0.54	0.49	0.55	0.51
2 km	0.48	0.43	0.50	0.43
6 h total precipitation				
15 km	0.67	0.59	0.65	0.53
5 km	0.65	0.44	0.62	0.42
2 km	0.49	0.42	0.49	0.38

The observed 2 m air temperature correlated well with all model simulations and at all horizontal resolutions, with a coefficient of $r > 0.89$. REF and IDAE better represented air temperature changes at 15 km resolution, reaching $r = 0.96$, while the coefficients with DAE and COMB were the lowest. There are no differences among runs at 5 and 2 km resolutions. Statistical errors of model simulations showed improved results for REF and IDAE at 15 km resolution compared with DAE and COMB at the same resolution (see Table A1).

The Enviro-HIRLAM model rather well reflects 2 m relative humidity variability with a correlation of $r > 0.81$ (Table 1). Similarly to the 2 m air temperature, REF and IDAE better simulated the observed conditions at 15 km spatial resolution. However, there are practically no differences in the results at finer resolutions. The highest values of errors were identified for DAE and COMB at 15 km, whereas the best results showed IDAEs at 15 and 2 km resolutions (Table A1).

The correlations for the 10 m wind speed varied from $r = 0.67$ to $r = 0.82$ (Table 1). At a coarse 15 km resolution, DAE and COMB showed lower, but strong, values of correlation coefficients, mainly because of the enhanced direct aerosol effects. Nevertheless, while spatial detailing improved and wind differences became more heterogeneous, the correlation with COMB significantly increased, and at 2 km resolution, it became as high as the IDAE. The highest errors were identified for COMB at 15 km, and the lowest errors for COMB at 2 km resolution (Table A1).

Modeled total cloud cover and precipitation, as in many meteorological model simulations, did not always show satisfactory results. Moreover, depending on the specific

meteorological situation and irregular patterns in the formation and development of clouds and precipitation, correlation sometimes decreases with a finer spatial resolution (see Table 1). One of the challenges is related to a lack of accurate cloud cover measurements at synoptic stations. For example, the cloudiness is defined visually with a one-point accuracy (0 points for a clear sky is a minimum, and 10 points for 100% coverage is a maximum). Furthermore, precipitation is measured with a 0.5 mm accuracy. Another challenge is linked to slight shifts in the spatial location of precipitation or cloudiness maxima for the runs with more detailed resolution. Better results were found for REF and IDAE with $r = 0.67$. Overall, the total cloud cover was better modeled for REF at 15 km compared with 2 km resolution for all runs with aerosol effects included. Precipitation was better simulated for REF and IDAE at 15 and 5 km resolution. At the same time, the simulations with both aerosol effects (COMB) showed the lowest correlations with the observations (Table A1).

The performed modeling of temperature, moisture, and wind showed acceptable results and higher accuracy in the simulations for the period 5–29 April 2020. The rather crude measurements of raw meteorological observations for the total cloud cover and precipitation might be a possible reason for the lower performance. Therefore, this should be considered during further analysis. Verification of the model results for different Enviro-HIRLAM model runs with the aerosol effects included showed better results for the wind speed (for all DAE, IDAE, and COMB runs) and the total cloud cover (for IDAE run). Hence, the simulated distribution of wind and cloudiness during the studied period was dependent on the aerosol feedback and interactions in the atmosphere. At the same time, over the entire period, the results did not show a clear influence of aerosols on the air temperature, relative humidity, or precipitation.

3.2. Modeled Weather Conditions without Aerosol Effects

This section is focused on the distribution of modeled meteorological parameters based on the REF run without including the aerosol effects. Considering the meteorological analysis of the synoptical situation in Section 2.5, this section helps to determine the key features of 3D meteorological fields, dependence on horizontal resolution, and how meteorological parameters were distributed without the impact of aerosol direct and indirect effects. We focus on the air temperature and wind to analyze thermal and wind regimes, cloudiness, and precipitation during the study period. The relative humidity was not considered here, being computed at a 2 m height above ground as part of the classical set for NWP model verification. To analyze the 3D moisture regime and distinguish dry and wet weather conditions, we used specific humidity because it is available at all model levels.

3.2.1. Air Temperature

Although the air temperature was not exceptionally high during April 2020, it was the dry conditions that facilitated a rapid expansion of wildfires, which escalated from routine seasonal open burning to uncontrolled fires, as detailed by Savenets et al., 2020 [8]. During the period of wildfires, the air temperature varied from 5.0 °C to 10.0 °C near the surface in the northern part of Ukraine (Figure 3a). Sometimes, it dropped down to 0–1 °C at night and exceeded 20.0 °C at midday. The warmest days during the period of active wildfires were observed on 7–9 April, when the daily average air temperature varied from 9.3 °C to 11.0 °C, while on 13 April, the daily average temperature reached 12.7 °C and, on 16 April 2020, it was 11.0 °C. On these days, the activity of wildfires significantly intensified [8]. During the midday hours on these days, positive temperatures extended up to 3 km above the surface.

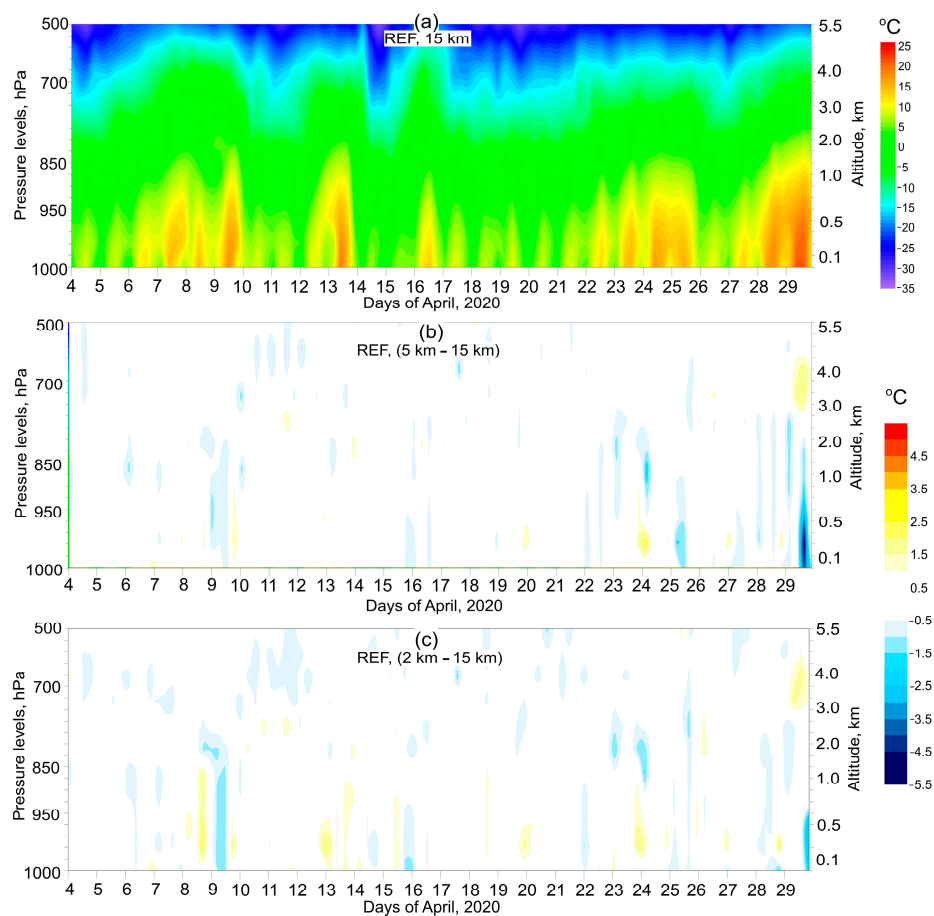


Figure 3. Time series (3 h temporal resolution) of the vertical cross-section (at pressure levels/altitudes) of air temperature (T , $^{\circ}\text{C}$) over wildfires area in the CEZ (for the Enviro-HIRLAM reference (REF) run for 15 km (a), and the difference between 5 km and 15 km (b), and 2 km and 15 km (c) horizontal resolutions).

Short-term cooling between the two wildfire periods resulted in a near-surface daily average air temperature drop to $3.4\text{--}8.1\text{ }^{\circ}\text{C}$ due to changes in the synoptic situation and activity of the weather fronts (see Section 2.5). In particular, the average air temperature dropped to $3.4\text{ }^{\circ}\text{C}$ on 14 April 2020 following precipitation that caused the wildfire episode to be divided into two parts. On 14 April 2020, wildfires were observed in the CEZ. However, new wildfires appeared in the north of the Zhytomyr region the day after. During 14–16 April, the differences between the midday and nighttime air temperatures near the surface were less than $6.0\text{ }^{\circ}\text{C}$, which was significantly smaller than those during the previous days.

Fortunately, the wildfire events ended before the nighttime air temperature rose to over $8\text{ }^{\circ}\text{C}$ after 27 April, which might have caused a disastrous impact on the flammable conditions. At the end of April, the daily average near-surface temperature reached $17.0\text{ }^{\circ}\text{C}$, with a daily maximum of $23.1\text{ }^{\circ}\text{C}$, and the positive air temperature extended up to 3 km above the surface (Figure 3a).

Increasing the horizontal resolution to 5 and 2 km mostly showed the same vertical distribution of air temperature (see Figure 3b,c). Sometimes, for some hours on a diurnal cycle in the warmer days, the air temperature in REF simulations with finer resolutions was up to $1.0\text{ }^{\circ}\text{C}$ lower in comparison to runs with a 15 km resolution. The highest differences were observed only on 29 April 2020, when the air temperature for 5 and 2 km was up to $3.8\text{ }^{\circ}\text{C}$ lower in the lowest layer of the troposphere.

3.2.2. Specific Humidity

It was found that the moisture content was rather low during the period of wildfires. Typical values for the specific humidity were lower than 3 g/kg (Figure 4a). Dry conditions were interrupted by short-term atmospheric front movement when the specific humidity exceeded 5 g/kg. The driest period was observed from 11 until 13 April, when specific humidity decreased to values to lower than 1.5 g/kg and supported the spread of wildfires. However, the fires were interrupted by an especially high moisture content observed during 13–14 April 2020, when the stationary atmospheric front passed through the studied region (see the details about the synoptic conditions in Section 2.5). This is exactly the process that caused the April 2020 wildfire period to be divided into two sub-periods with different areas of active wildfires. After the intense changes in the specific humidity during 14–17 April, the moisture content became more stable until the end of the wildfire period during 25–26 April. The specific humidity varied within 5–7 g/kg near the surface during the last days of the studied period, when the wildfires were already extinguished.

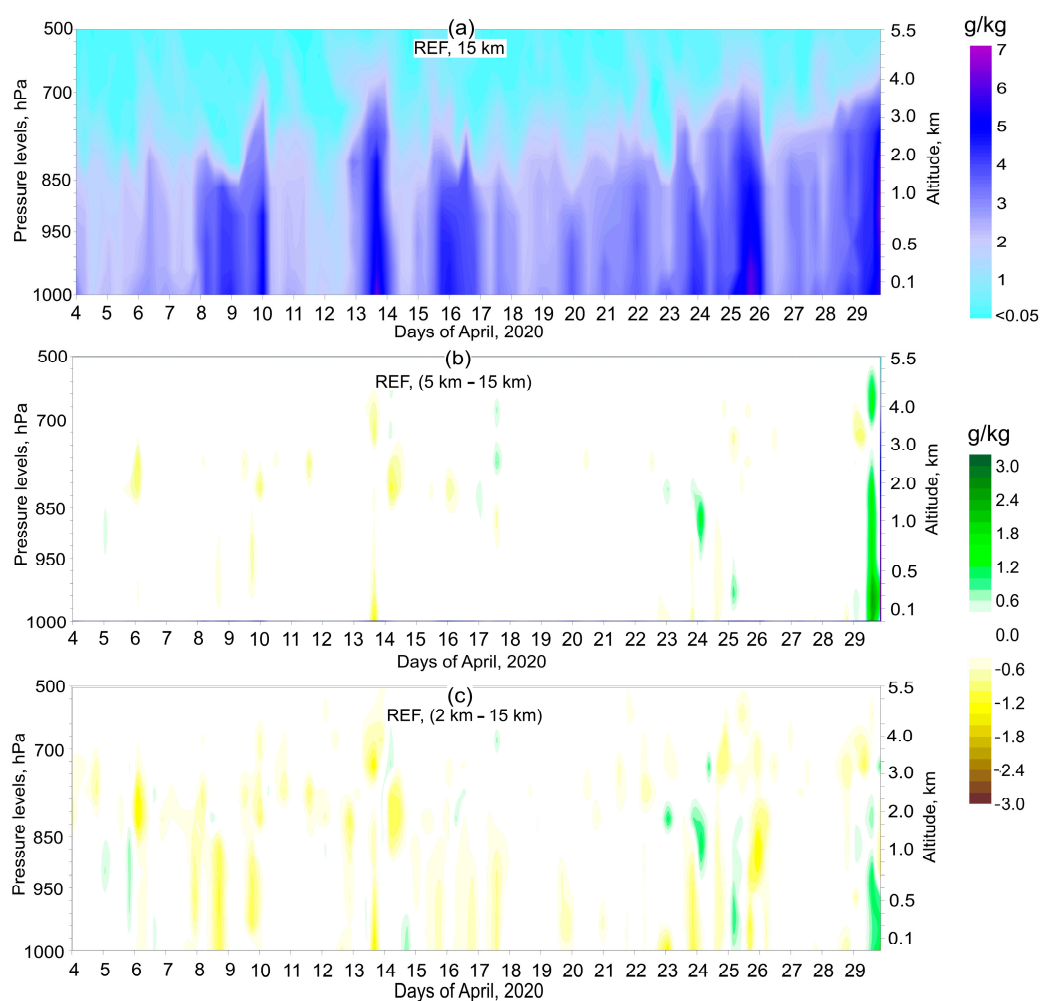


Figure 4. Time series (3 h temporal resolution) of the vertical cross-section (at pressure levels/altitudes) of specific humidity (g/kg) over wildfires area in the CEZ (for the Enviro-HIRLAM reference (REF) run for 15 km (a), and the difference between 5 km and 15 km (b), and 2 km and 15 km (c) horizontal resolutions).

As in the case of air temperature, the increase in horizontal resolution did not influence the vertical distribution of the specific humidity by much (Figure 4b,c). During the period of 6–23 April, the REF simulations with finer resolutions (especially 2 km) occasionally showed drier conditions at different altitudes (up to 3 km). In such hours, the specific humidity was 0.5–1.3 g/kg lower in comparison to the REF run at 15 km resolution. Modeling

with a finer resolution revealed that the moisture regime was more favorable for wildfires locally over the CEZ. As for the air temperature, the highest differences between the REF simulations were identified to take place on 29 April 2020, when the specific humidity at a 2 km resolution was 2.0 g/kg higher. Fortunately, the wildfires were already extinguished by that time.

3.2.3. Wind, Total Cloud Cover, and Precipitation

Prior to the advancement of the stationary front on 14 April 2020, the most severe wildfires were in the CEZ, not far from the Chernobyl nuclear power plant (CNPP). Precipitation with an intensity of up to 10 mm per 3 h (see Figure 5) helped firefighters extinguish wildfires in this area. The wind speed decreased from 7–8 m/s to 1–2 m/s after the stationary front passed through northern Ukraine.

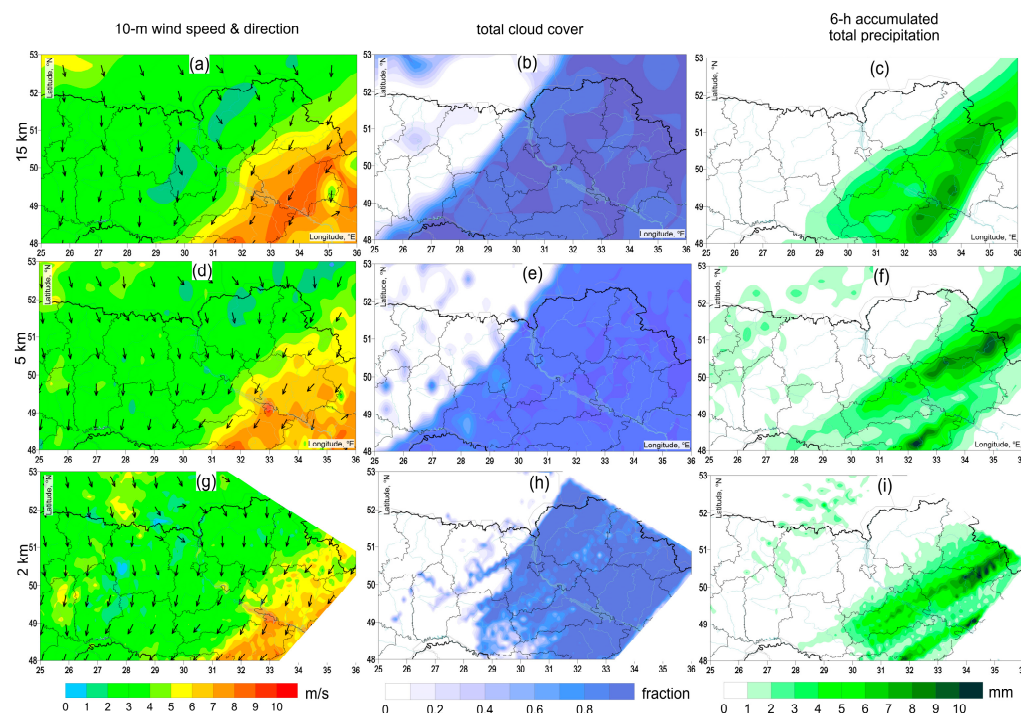


Figure 5. An example of Enviro-HIRLAM simulations over the area of interest for 10 m wind speed and direction (a,d,g), total cloud cover fraction (b,e,h), and 6 h accumulated total precipitation (c,f,i) which observed during atmospheric stationary front conditions on 14 April 2023 at 18 UTC (for REF run at 15 (a–c), 5 (d–f), and 2 (g–i) km horizontal resolutions; the area outside the 2 km domain (g–i) is shown as blank).

After 14 April 2020, the synoptic situation (see Section 2.5 and Figure 2) was favorable for the wind speed increase. New territories in the northern part of Ukraine started to burn with rapid fire spread, forming new wildfire hotspots. The burning area significantly decreased on 21 April 2020, and finally, the fires disappeared after rainfall during 25–26 April 2020.

An increase in horizontal resolution gave a more detailed picture of the spatial distribution of the meteorological fields (for example, Figure 5). At the same time, there were slight changes in the vertical distribution with increasing horizontal resolution (see Figures 3 and 4). The results of the REF simulations supported by the synoptic analysis (from Section 2.5) showed the necessity to pay specific attention to the frontal weather conditions on 14 April 2020. It caused the spatial redistribution of wildfires and differences in the spatio-temporal variability of meteorological parameters. We explore the concurrent aerosol effects and their spatial variability next.

3.3. Modeled Atmospheric Composition during the Wildfire Episode

To understand how the meteorological fields were modified by the direct and indirect aerosol effects, we should consider the modeled atmospheric composition and spatio-temporal distribution of different aerosol compounds. The observed aerosol effects on the meteorological parameters may vary depending on their concentrations, ratios, and certain weather conditions. This section focuses on the key features of aerosol distribution in the atmosphere during the April 2020 wildfire episode.

We simulated mass mixing ratios (as a concentration of a certain pollutant expressed in parts per billion (ppbm) or as a mass of pollutant in a mass of air, thereafter concentration) for the wildfire period in Ukraine. The case study was characterized by elevated BC and OC concentrations due to forest fires observed in the CEZ. This underscores the necessity for spatio-temporal aerosol analysis prior to assessing aerosol effects in the atmosphere. In the study region affected by wildfires, four primary aerosol types were identified with significant concentrations: BC, OC, dust, and sulfates (Figure 6). Sea salt was the only aerosol component with a ratio among other compounds less than 0.01%, mainly because of the longer distance to marine areas, and hence with a negligible contribution. Near the surface, sulfates accounted for 13% of all aerosol compounds, while dust accounted for about 7%. With the altitude increase, sulfates and dust content gradually increased, with a maximum at approximately 1.5–2.0 km (900–850 hPa) above the surface that, on average, corresponded to the top level of the boundary layer. At these heights, sulfate concentration reached a maximum of 18.8%, while the dust contribution was 12.1%.

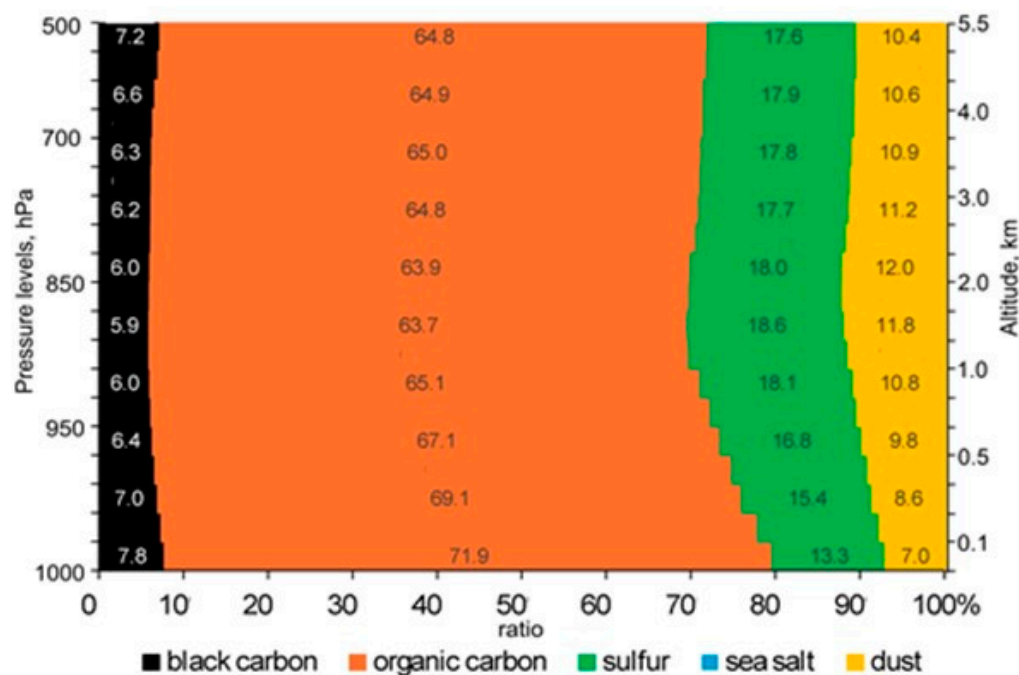


Figure 6. Vertical distribution of the modeled ratio of aerosol compounds over CEZ averaged over 5–29 April 2020. Note that sea salt contribution is negligible, being less than 0.01%.

During wildfires in the CEZ, the maximum BC and OC concentrations observed near the surface accounted for 7.8% and 71.9%, respectively (Figure 6). In the lowest 5 km layer, OC was the prevailing aerosol component, reaching at least 63.7% among all aerosol compounds. The layer at altitudes 1–3 km above the surface was characterized by a minimum carbonaceous aerosol content, forming two layers with higher concentrations below (as a result of local wildfire emissions) and above (as a result of atmospheric transport from other regions).

In general, the average OC content near the ground reached 2.6 ppbm, being rather equally distributed up to 2.5 km (about 800 hPa) (see Figure A6). At higher altitudes, the

OC content gradually decreased to 1.0 ppbm at a 5 km height (about 500 hPa). At night, the OC content exceeded 3.0 ppbm in the lower troposphere because of the higher atmospheric stability. Starting from 0.1–0.3 km above the surface, the OC content was higher during daytime hours under more favorable conditions for pollution dispersion from the lowest atmospheric levels. The same behavior was typical for BC. However, the content was significantly lower, being 0.25 ppbm on average and reaching 0.30 ppbm at night near the surface.

The accumulation mode was the main aerosol size at almost all altitudes and all hours, reaching 1.4–2.5 ppbm for OC and 0.13–0.25 ppbm for BC in the lowest 3 km layer (see Figure 7). The Aitken mode mainly varied from 0.4 to 1.0 ppbm for OC and from 0.04 to 0.11 for BC. Both the BC and OC coarse modes did not exceed 2.0×10^{-4} ppbm on average.

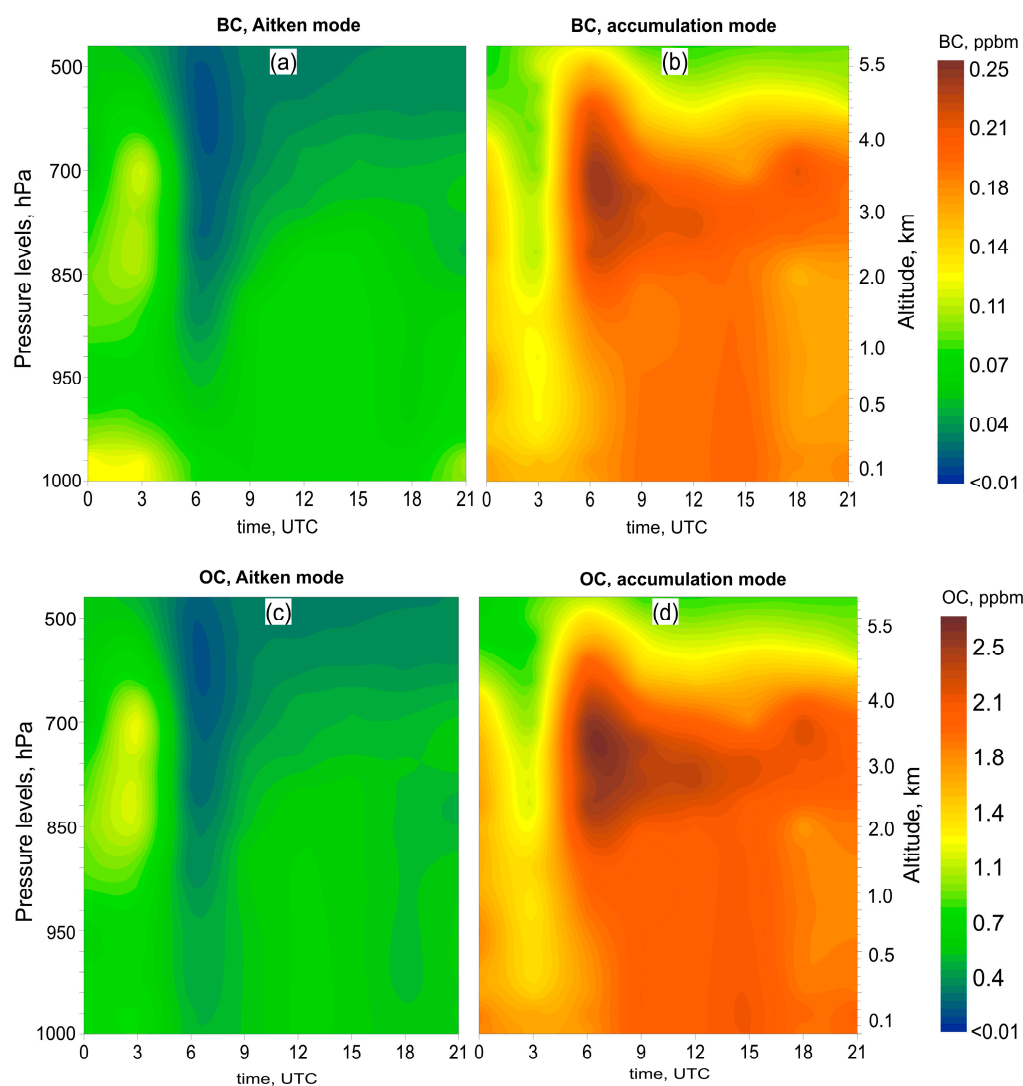


Figure 7. Diurnal cycle (over 5–29 April 2020) of the vertical cross-section (at pressure levels/altitudes) over wildfires in the CEZ of modeled BC (a,b) and OC (c,d) for the Aitken and accumulation modes. The color scales for BC and OC are different for better visibility.

Carbonaceous aerosols had clearly visible diurnal variations, showing different behaviors with the height above the surface (Figure 7). At night, from 00 to 03 UTC (from 03 to 06 a.m. local time), a decrease in concentrations for the BC and OC accumulation mode above 2 km (≈ 850 hPa) was observed (Figure 7b,c). At the same time, the Aitken mode exceeded the accumulation mode in the layer at 2–4 km (≈ 850 –700 hPa). In the early morning, the BC and OC accumulation modes rapidly increased, while the Aitken

mode decreased to its diurnal minimum. The highest BC and OC accumulation mode concentrations were located approximately 3 km above the surface. This layer was typically observed during a day from 06 to 18 UTC (from 09 a.m. to 09 p.m. local time). The coarse mode was observed mainly from 00 to 09 UTC (from 03 to 12 a.m. local time) in the lowest 1 km layer.

3.4. Direct and Indirect Aerosol Effects on the Atmosphere

This section deals with direct and indirect aerosol effects on the distribution of meteorological parameters based on the results of the DAE, IDAE, and COMB model simulations. We explore the results by studying the differences between the simulated meteorological fields with the aerosol effects turned on against the reference (REF) simulation (Figure 8).

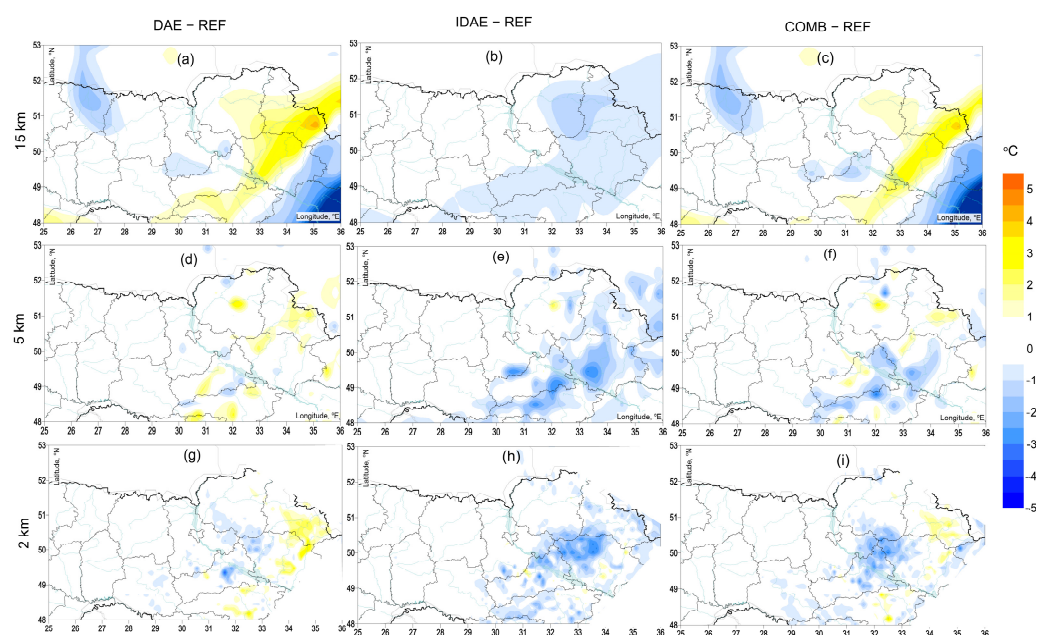


Figure 8. Difference between the Enviro-HIRLAM modified (with aerosol effects) and reference (control) runs for direct (DAE) (a,d,g), indirect (IDAE) (b,e,h), and combined (COMB) (c,f,i) aerosol effects on 2 m air temperature on 10 April 2020 at 12 UTC.

The modeling results show that aerosol effects were inhomogeneous in time and space over the region of study. Depending on weather conditions, even the opposite effects were observed, especially during frontal activity. However, despite the spatio-temporal heterogeneity, the overall changes in meteorological parameters had similar features during the days without active frontal processes. Based on our analysis for the period 4–29 April 2020, we focused primarily on two periods: 10 April 2020, representing common features of direct and indirect aerosol effects during wildfires, and 14 April 2020, representing aerosol effects during cold fronts, which resulted in wildfire redistribution. Figures 8–16 represent the key changes in the selected meteorological parameters.

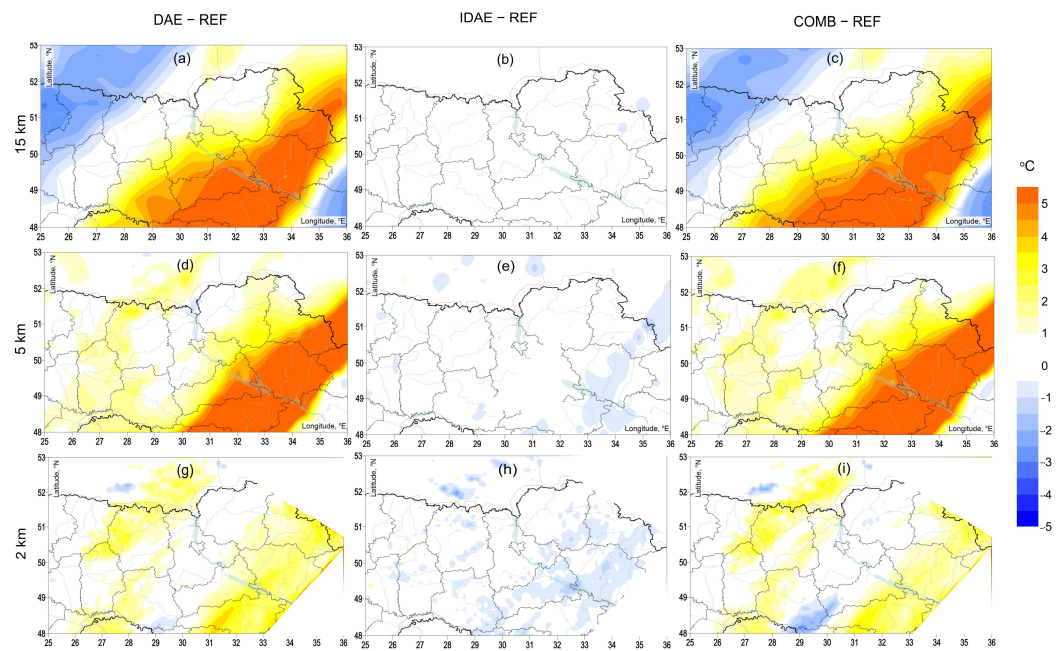


Figure 9. Difference between the Enviro-HIRLAM modified (with aerosol effects) and reference (control) runs for direct (DAE) (a,d,g), indirect (IDAE) (b,e,h), and combined (COMB) (c,f,i) aerosol effects on 2 m air temperature on 14 April 2020 at 18 UTC.

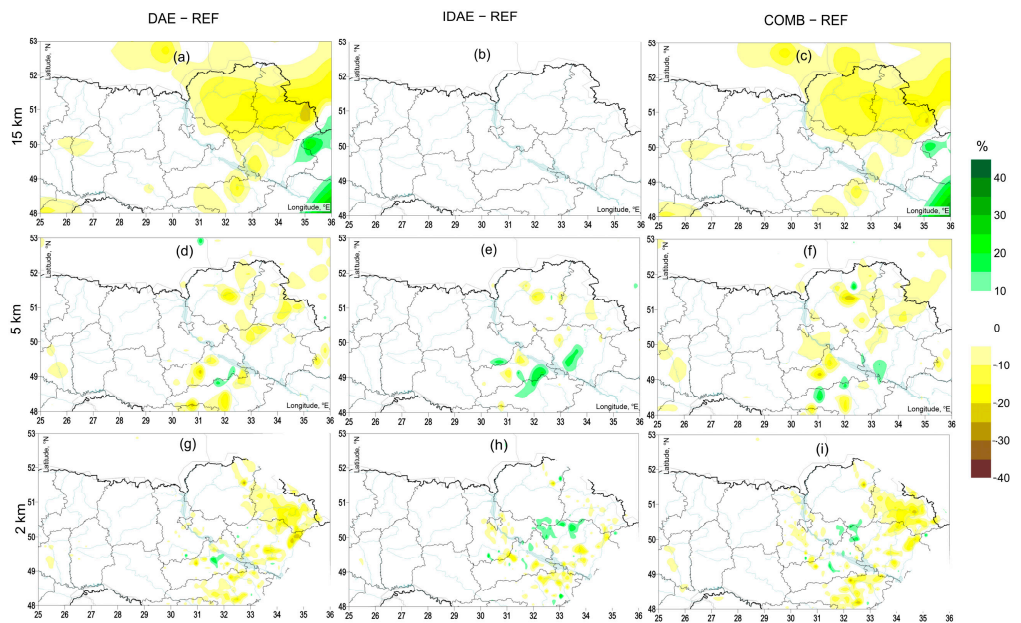


Figure 10. Difference between the Enviro-HIRLAM modified (with aerosol effects) and reference (control) runs for direct (DAE) (a,d,g), indirect (IDAE) (b,e,h), and combined (COMB) (c,f,i) aerosol effects on 2 m relative humidity on 10 April 2020 at 12 UTC.

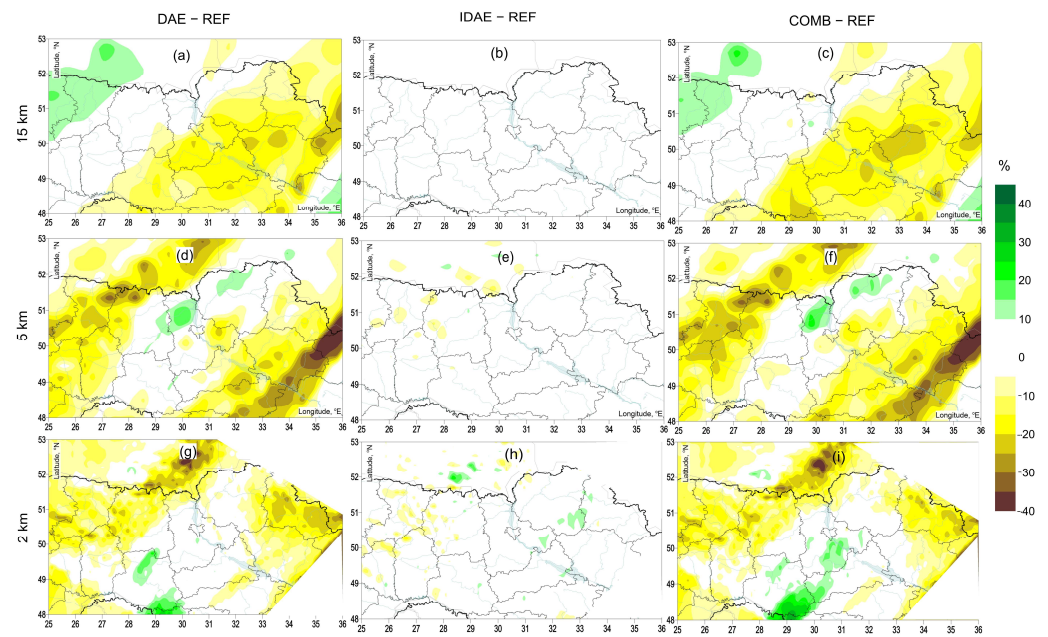


Figure 11. Difference between the Enviro-HIRLAM modified (with aerosol effects) and reference (control) runs for direct (DAE) (a,d,g), indirect (IDAE) (b,e,h), and combined (COMB) (c,f,i) aerosol effects on 2 m relative humidity on 14 April 2020 at 18 UTC.

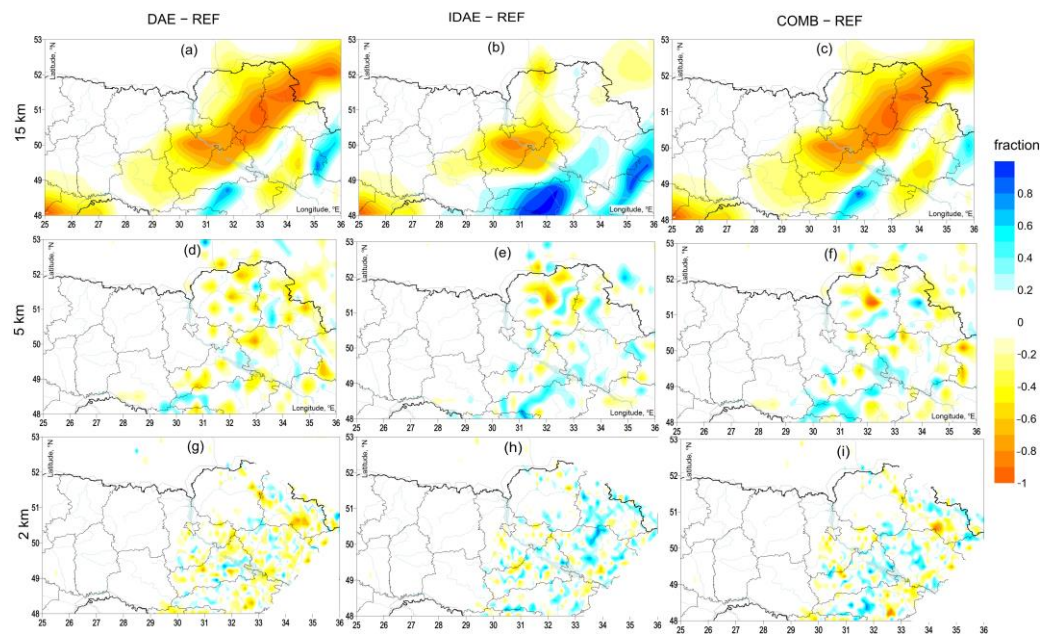


Figure 12. Difference between the Enviro-HIRLAM modified (with aerosol effects) and reference (control) runs for direct (DAE) (a,d,g), indirect (IDAE) (b,e,h), and combined (COMB) (c,f,i) aerosol effects on total cloud cover on 10 April 2020 at 12 UTC.

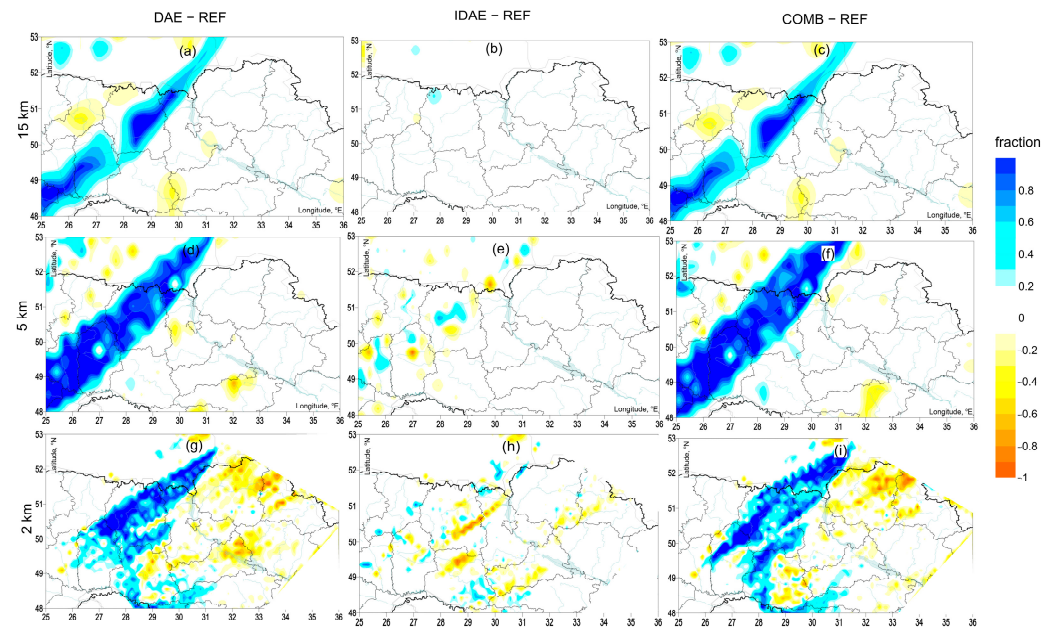


Figure 13. Difference between the Enviro-HIRLAM modified (with aerosol effects) and reference (control) runs for direct (DAE) (a,d,g), indirect (IDAE) (b,e,h), and combined (COMB) (c,f,i) aerosol effects on total cloud cover on 14 April 2020 at 18 UTC.

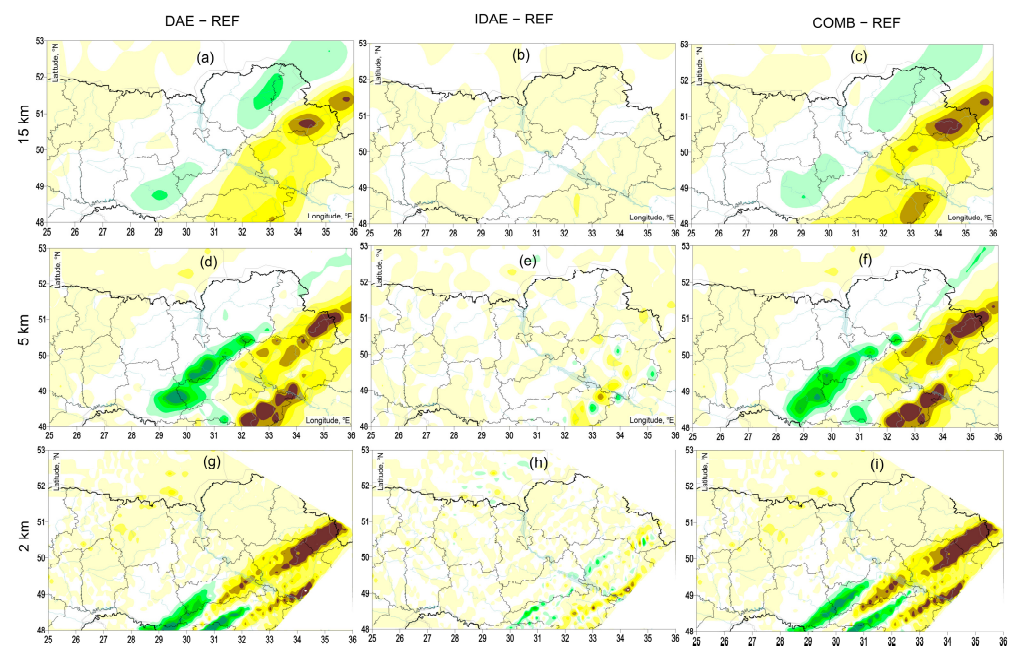


Figure 14. Difference between the Enviro-HIRLAM modified (with aerosol effects) and reference (control) runs for direct (DAE) (a,d,g), indirect (IDAE) (b,e,h), and combined (COMB) (c,f,i) aerosol effects on total precipitation on 14 April 2020 at 18 UTC.

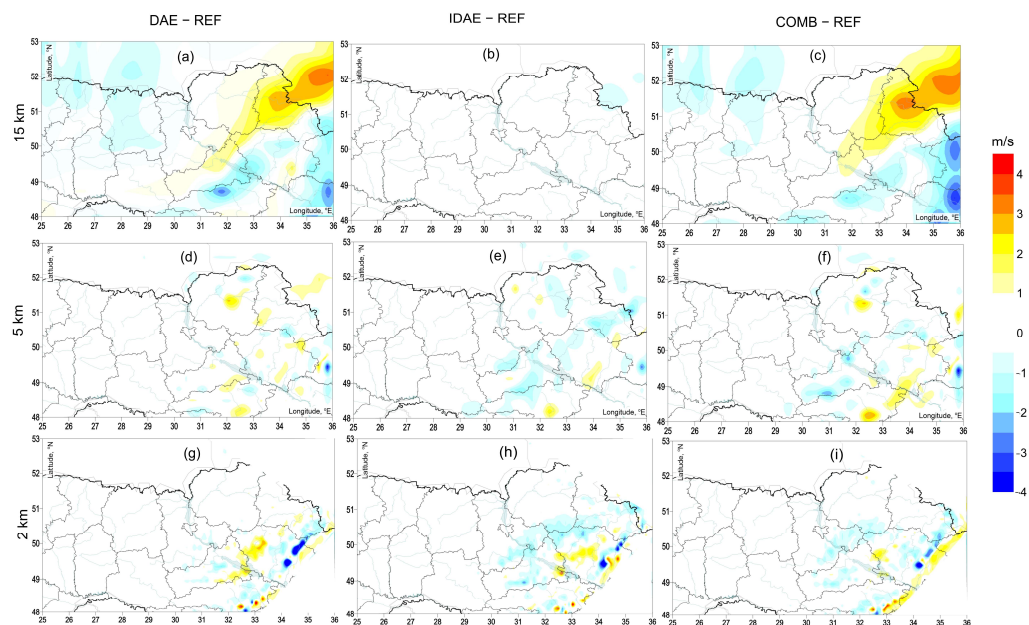


Figure 15. Difference between the Enviro-HIRLAM modified (with aerosol effects) and reference (control) runs for direct (DAE) (a,d,g), indirect (IDAE) (b,e,h), and combined (COMB) (c,f,i) aerosol effects on 10 m wind speed on 10 April 2020 at 12 UTC.

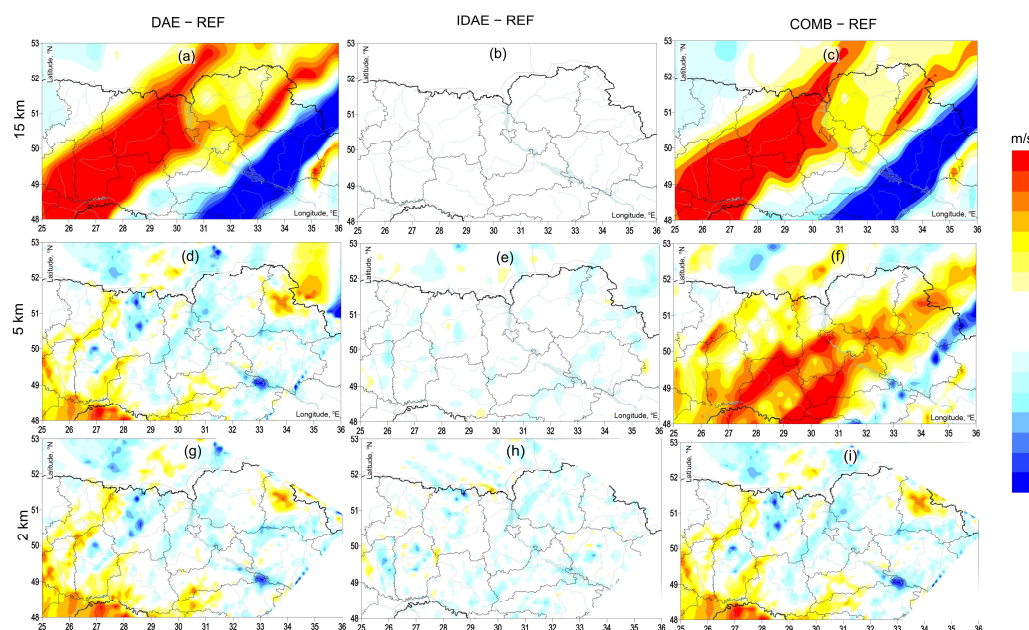


Figure 16. Difference between the Enviro-HIRLAM modified (with aerosol effects) and reference (control) runs for direct (DAE) (a,d,g), indirect (IDAE) (b,e,h), and combined (COMB) (c,f,i) aerosol effects on 10 m wind speed on 14 April 2020 at 18 UTC.

During the wildfire episode, aerosol effects on average resulted in slightly colder weather for model runs at coarser horizontal resolutions. These effects mostly disappeared at a finer resolution. Direct aerosol effects were so strong that they largely determined the general aerosol impact obtained by the COMB run. Typically, under more stable weather conditions, DAE contributed to the 2 m air temperature by $\pm 4\text{ }^{\circ}\text{C}$ at a 15 km horizontal resolution (Figures 8 and 9).

Modeling with a finer resolution showed less noticeable changes in temperature (up to $\pm 2\text{ }^{\circ}\text{C}$) with a more heterogeneous spatial distribution. A colder 2 m air temperature was the result of indirect aerosol effects, with more intense cooling (up to $-3\text{ }^{\circ}\text{C}$) detected

at a finer resolution. Since the changes in IDAE are negligible compared to DAE, the COMB simulation mirrors the changes in DAE. Our results show that atmospheric fronts enhance aerosol effects in the atmosphere (as seen in Figure 9). DAE showed a strong warming of more than 5 °C over a large area in the south-east, even for 2 km spatial resolution. IDAEs during atmospheric front passage (Figure 9b,e,h) were less visible in comparison to more stable weather conditions (Figure 8b,e,h). As OC and BC accounted for more than 70% of all aerosol compounds (see Figure 6) during the wildfire episode, such strong aerosol effects appeared because of their prevailing impact. The analysis showed that it is better to consider the REF or IDAE runs at the coarse resolution, indicating that the OC and BC impacts on 2 m air temperature might be overestimated. However, at a smaller scale, all model simulations with aerosol effects better represent the observed air temperature changes.

Aerosol effects during the wildfires resulted in mostly drier conditions (see Figures 10 and 11) over the areas that corresponded to certain air temperature changes. While IDAE showed very slight effects for both more stable and changeable weather conditions, DAE-driven changes were significant, especially during atmospheric cold front movement. The 2 m relative humidity was 20% lower for the majority of the studied period in comparison to the REF simulations (see the region in the north-east of Ukraine in Figure 10). However, the humidity values were approximately 40% lower during intense frontal processes (Figure 11d,f,g,i). The inconsistency of aerosol effects on the relative humidity among different horizontal resolutions was detected on 14 April 2020 (Figure 11). At 15 km resolution, DAE (Figure 11a) and COMB (Figure 11c) were less intense with respect to the relative humidity, with almost a 20% decrease. Moreover, an increase up to 15% in the relative humidity was observed in the north-west. This relative humidity increase in the north-west was not seen in the 5 km model simulation but shifted to an area near Kyiv (Figure 11d,f). The relative humidity decreased by almost 40% and was considerably drier near the atmospheric front. At 2 km resolution, we observed another pattern in comparison to the 5 and 15 km runs, with lower values of the relative humidity shifting towards the south-east for DAE and COMB (Figure 11g,i) and up to +40% higher relative humidity air between the two zones of low relative humidity for COMB simulation.

Similarly to the 2 m air temperature, the verification results showed an overestimation of aerosol effects for the 2 m relative humidity. As seen in Figures 8–11, the areas with higher 2 m air temperatures corresponded to lower 2 m relative humidity. Considering the high BC and OC ratios among the aerosol compounds during the wildfire episode, the modeled aerosol effects were too enhanced, making the REF and IDAE model runs more realistic.

On average, aerosol effects caused total cloudiness to decrease. However, taking into account specific time periods and areas, the impact of aerosol content on the total cloud cover varied a lot during wildfires for all model simulations (Figures 12 and 13). At a finer resolution, the results indicated spatially separated cells with opposite effects. However, at 15 km resolution, the differences were distributed much more uniformly, covering large areas with prevailing increased or decreased total cloud cover (see Figure 12a–c). A more uniform field at coarser resolution better corresponded to the observed total cloud cover changes. IDAE model simulations showed weaker aerosol effects, being closer to the observed conditions. Overall, the total cloud cover fraction differed from REF by up to ± 0.8 . It is very arguable that aerosol effects caused such significant changes because of their direct impact on cloud formation. The reason for the most extreme changes in cloud cover was its redistribution because of changes in wind speed, so the same cloud cells were shifted from their locations modeled in the REF run. It was found out that DAE showed more intense cloud formation after the passage of the atmospheric occluded fronts. Such a feature is presented, e.g., in the lines of the increasing cloud fraction over the western and north-western areas in Figure 13. More clouds during the atmospheric front movement formed in areas with more intense wind speed changes (see north and north-western areas in Figure 16) due to aerosol effects with no consequent changes in precipitation. The modeled indirect aerosol effects on the cloudiness showed better results than the REF run,

mainly because BC and OC were distributed in the lowest 4 km layer (as seen in Figure 7), where cloudiness actively forms, and these processes strongly depended on the aerosol chemical composition.

On average, an elevated aerosol content caused precipitation to increase. However, in many areas, precipitation decreased during unstable weather conditions, i.e., during atmospheric front movement. Because of the indirect aerosol effects, accumulated precipitation decreased by 4 mm per 6 h in the days with cold and occlusion fronts, as seen over the eastern areas in Figure 14. Direct aerosol effects caused more significant changes up to -8 mm per 6 h, especially in areas where the relative humidity was lower. Furthermore, at the edge of atmospheric fronts, precipitation increased even though there were no significant changes in the total cloud cover.

The aerosol effects resulted primarily in an increase in wind speed, however varying locally. The model showed especially strong direct aerosol effects for the coarse 15 km horizontal resolution (Figures 15 and 16). However, these simulations did not reflect the observed wind conditions (see Section 3.1). The wind speed distribution simulated at 2 km resolution in both REF and IDAE was closer to the observations. Aerosol effects on the wind speed caused local changes up to ± 4 m/s. Wind speed at 10 m was the only parameter for which all model simulations with aerosol effects showed a better agreement with the observed data in comparison to the REF mode. Moreover, this agreement increased with a detailed horizontal resolution.

4. Discussion

Although wildfire emissions are often observed over the region of study, the vertical distribution of carbonaceous aerosols (BC and OC), ratio of their particle size, and other features can be different. For example, a previous case study performed using the Enviro-HIRLAM modeling system for 2010 wildfire events [31] showed numerous significant differences. While the accumulation mode was dominant in both the presented and previous studies, the concentrations of Aitken and coarse aerosol particles were the opposite. The vertical distribution of BC and OC depended on the synoptic situation and the distance to the wildfires. These cases showed the necessity of expanding the diversity of additional case studies. Furthermore, a full picture of how fires in ecosystems (wildfires and agricultural burning) impact carbonaceous aerosol distribution and what the aerosol effects are on the atmosphere in general is still needed.

Our results show that the aerosol effects influenced the meteorological parameters near the surface. Most of the earlier studies have reported cooling effects due to the aerosols emitted from the wildfires [18–20,31]. In general, an elevated aerosol content (with prevailing BC and OC compounds) caused slight cooling, with greater agreement with a fine spatial resolution. Nevertheless, changes up to ± 4 °C were detected at a local scale or during specific synoptic conditions. Our previous study, conducted during more severe wildfires in 2010 but at some distance from burning areas [31], showed similar changes in the 2 m air temperature, reaching ± 3 °C. Ref. [33] described that opposite air temperature changes can be even more significant, reaching up to ± 6 °C at the local scale.

The relative humidity mostly decreased because of the aerosol effects during the studied wildfire episode, with opposite effects in some local areas. This can be the response to air temperature changes, with the spatial distribution of difference fields in Figures 8–11 showing the inverse relationship. The obtained results better corresponded with the changes indicated by the earlier study of Hodnebrog et al. (2016) [15]. However, the prevailing increase in the relative humidity once aerosol processes were included was shown in Xu et al. (2021) [20], which influenced aerosol distribution and precipitation changes [21]. Due to the aerosol effects, the changes in the wind speed reached ± 4 m/s in comparison to the reference run. The detected changes were comparatively large and not unidirectional, as also identified in [34].

Our results agreed with those already known (for example, [24,28,33]) about the impossibility of detecting simple relationships with cloudiness and precipitation changes.

The challenge is not only connected with the accuracy of the parametrizations used in the models. Another problem is distinguishing between the aerosol impact on the cloud-precipitation interaction and the shift in cloudiness and precipitation patterns due to wind changes caused by aerosol effects. A finer horizontal resolution often showed weaker aerosol impacts on meteorological parameters. The downscaling procedure revealed local variability in the distribution of the meteorological parameters. As a result, the observed aerosol effects became more heterogeneous in space but less strong.

All the analyzed changes in the meteorological parameters under stable weather conditions can be totally different during atmospheric frontal processes. We showed that the aerosol impacts during the passage of the atmospheric fronts were especially pronounced. Moreover, such conditions can modify hazardous events, influencing aerosol emissions and deposition. This points towards a need to place more attention in future studies on the seasonal difference in the aerosol impacts during the warm, cold, and occluded atmospheric fronts. While much attention is paid to convective processes (for example, [23,28]), the aerosol effects during frontal activity in high and midlatitudes require more comparison and verification. This is further justified because these atmospheric processes prevail over the mentioned latitudinal belts and mostly influence the regional weather.

We obtained quite large errors for DAE, especially for the 15 km spatial resolution. The modeled effects showed too-sharp changes in the meteorological parameters. The problem of the exaggerated role of aerosol effects frequently appears, as already shown in [29]. However, further sensitivity studies for different synoptic conditions over specific climate zones are needed to find the exact reason that for these problems in parameterization [27] may originate due to uncertainties in emission inventories [35].

The presented case study reflects the difficulties for firefighters and emergency services to overcome natural hazards in remote and contaminated areas like the CEZ. Since the Russia–Ukraine war started in 2022, the CEZ itself as well as a lot of other areas have become mined, hard to reach, and abandoned. Huge efforts must be put toward preventing negative consequences that might happen in the future when wildfires appear in these zones. It is very important for decision-makers to implement as many technical developments and measures as possible for monitoring, prediction, and analysis of the environmental situation. Seamless modeling can play a significant role as a powerful instrument to simultaneously predict weather conditions and estimate possible negative impacts of pollutants' emissions in the region of interest. These scientifically based improvements require the broadening of research, covering more historical cases of natural disasters with a focus on complex feedback and interactions between the land surface and the atmosphere above.

5. Conclusions

The April 2020 wildfire episode in Ukraine appeared as a joint consequence of several factors, namely anthropogenic (seasonal open burning) and natural (weather conditions) factors. Although the air temperature was not very high, rather dry conditions influenced the severity of the wildfires that governed aerosol emissions in the region. In the CEZ, the concentrations of BC and OC, mostly their accumulation mode, accounted for 80% of all aerosol components in the lowest atmospheric layer. The studied direct and indirect aerosol effects occurred under the observed aerosol ratios. In the layer 2–4 km above the surface, the largest variability of BC and OC was observed. This was the layer where the Aitken mode concentrations exceeded the accumulation mode concentrations at nighttime hours by 0.04 ppbm and 0.4 ppbm, respectively, followed by rapid changes in the BC and OC content (increases in the accumulation mode up to 0.24 ppbm and 2.5 ppbm, respectively) and consequent changes in the aerosol size distribution during the morning hours.

At low (15 km) horizontal resolution, the direct aerosol effects were overestimated, resulting in worse agreement of DAE and COMB simulations with the observations. The elevated content of carbonaceous aerosols emitted from the CEZ leads to colder and drier conditions. At a finer resolution, local features appeared, showing a 2 m air temperature decrease by 3 °C and a 2 m relative humidity drop by 20% in comparison to the REF

simulation. The most variable (and often opposite) influences were observed during atmospheric fronts. In general, the aerosol effects caused a great variety of changes in total cloud cover and accumulated precipitation. At the edges of the atmospheric fronts, the areas with precipitation increased, even though there were no significant changes in cloudiness. Some changes in the location of the cloudiness and precipitation patterns corresponded to spatial shifts in these patterns in the simulations with aerosol effects.

The results of this study showed that aerosol effects had a visible impact on the selected meteorological parameters. The aerosol effects were crucial for an improved spatio-temporal distribution of total cloud cover and variability of wind speed, showing the necessity of aerosol effect inclusion for better quality of atmospheric modeling. At the same time, large uncertainties were typical for direct aerosol effects caused by BC and OC, especially for modeling at coarse horizontal resolution. Although, in some meteorological situations, the effects of aerosols in NWP modeling might not be significant, in other cases, the anthropogenic influence, e.g., aerosol effects from forest fires, can play an important role in the modeling of regional meteorology. The detected tendencies towards drier conditions, local wind speed increases in some areas, and spatial shifts in cloudiness and precipitation patterns showed the necessity of operational assessments during wildfire episodes. These observed changes, forced by elevated aerosol content, can lead to unfavorable weather conditions. An improved prediction is critical for, e.g., early warning assessments in order to make science-based conclusions in decision-making and for the efficient use of resources by emergency services during natural disasters.

Author Contributions: Conceptualization, M.S. and A.M.; methodology, M.S., A.M. and R.N.; formal analysis, M.S. and V.R.; investigation, M.S. and V.R.; writing—original draft preparation, M.S.; writing—review and editing, A.M., R.N., A.B., M.K. and T.P.; visualization, M.S.; supervision, A.M.; project administration, A.M., M.K. and T.P. All authors have read and agreed to the published version of the manuscript.

Funding: The work has been performed under the Project HPC-EUROPA3 (INFRAIA-2016-1-730897), obtained while conducting the project “Integrated modelling for assessment of potential pollution regional atmospheric transport as result of accidental wildfires” (2020–2022). The work has been partially supported by the Atmosphere and Climate Competence Center (ACCC) Flagship via Research Council of Finland (no. 337549); the project “Research Infrastructures Services Reinforcing air quality monitoring capacities in European URBAN & Industrial areas” (RI-URBANS), no. 101036245; and the project “Research and development for integrated meteorology—atmospheric composition multi-scales and—processes modelling for the Pan-Eurasian EXperiment (PEEX) domain for weather, air quality and climate applications” (Enviro-PEEX(Plus) on ECMWF).

Institutional Review Board Statement: Not applicable.

Informed Consent Statement: Not applicable.

Data Availability Statement: The Enviro-HIRLAM modeling system is a community model. The source code is available for non-commercial use (i.e., research, development, and science education) upon agreement through contact with Alexander Mahura (alexander.mahura@helsinki.fi), Bent Sass (bhs@dmi.dk), and Roman Nuterman (nuterman@nbi.ku.dk). Documentation is available from <http://hirlam.org>, <http://hirlam.org/index.php/documentation/chemistry-branch> (accessed on 25 January 2024). The generated Enviro-HIRLAM model output for the studied period has a size of 2 Tb, and it is available upon request (contact Mykhailo Savenets, savenets@uhmi.org.ua). The archives of source meteorological data measured at synoptic stations can be provided by the Central Geophysical Observatory named after Boris Sreznnevsky (Kyiv, Ukraine) on request. The meteorological data of the synoptic stations located in Belarus were downloaded from <http://www.meteomanz.com/index?l=1> (accessed on 25 January 2024).

Acknowledgments: The authors gratefully acknowledge the computer resources and technical support provided by the Center for Science Computing (CSC) HPC (Finland). This study was carried out within the framework of the State Emergency Service of Ukraine and National Academy of Sciences of Ukraine. We acknowledge the Central Geophysical Observatory named after Boris Sreznnevsky (Kyiv, Ukraine) for providing the archived meteorological data measured at Ukrainian

synoptic stations. The authors thank the reviewers for their valuable comments and suggestions that helped to improve the paper. Open access funding provided by University of Helsinki.

Conflicts of Interest: The authors declare no conflicts of interest.

Appendix A

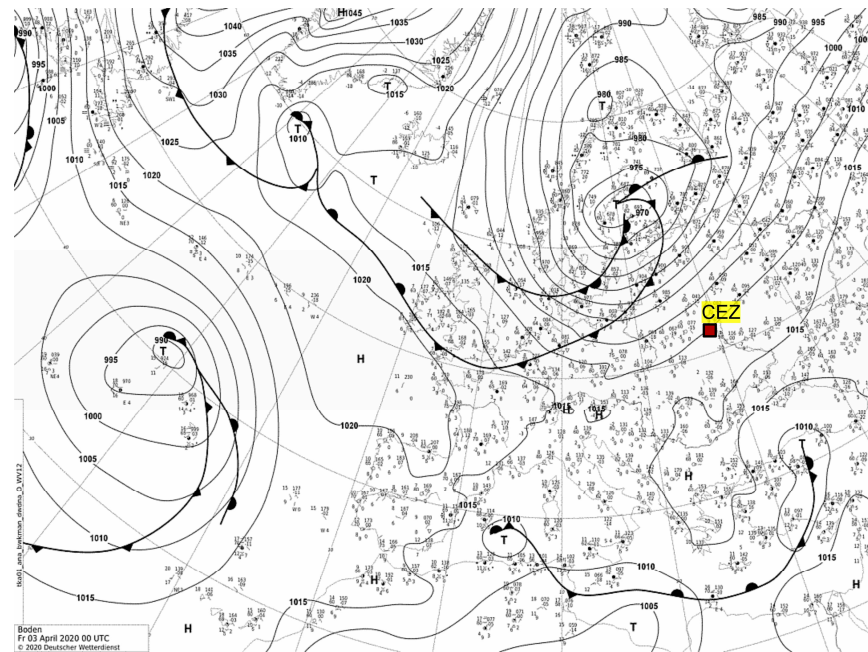


Figure A1. DWD archive synoptic map at 00 UTC on 3 April 2020 (source https://www.wetter3.de/archiv_dwd_dt.html (accessed on 13 October 2023)), with the red square corresponding to the CEZ location.

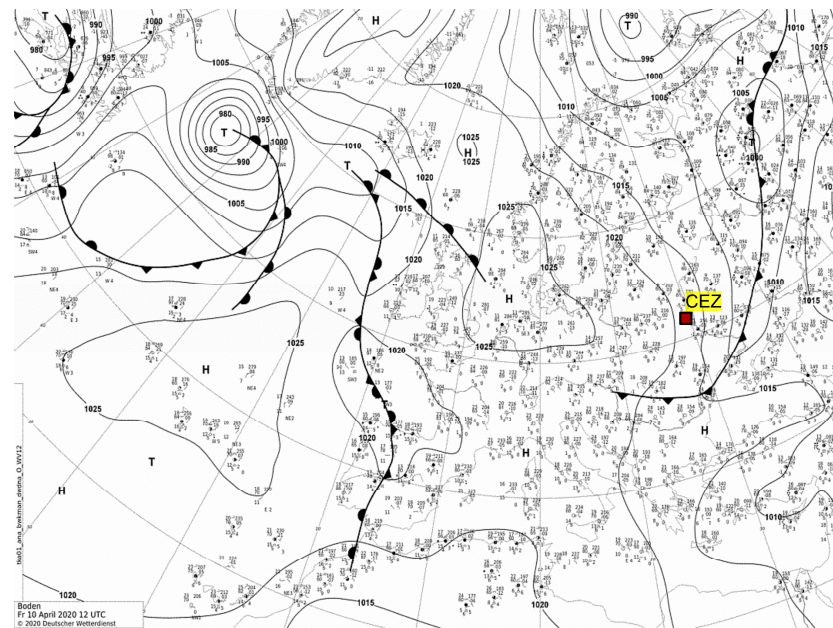


Figure A2. DWD archive synoptic map at 12 UTC on 10 April 2020 (source https://www.wetter3.de/archiv_dwd_dt.html (accessed on 13 October 2023)), with the red square corresponding to the CEZ location.

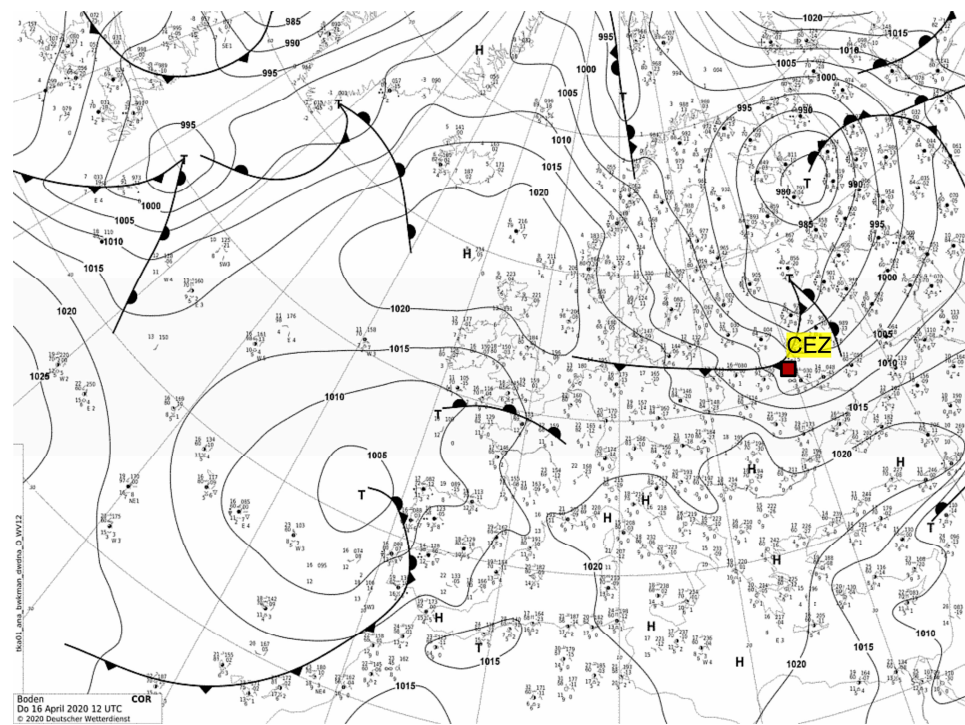


Figure A3. DWD archive synoptic map at 12 UTC on 16 April 2020 (source https://www.wetter3.de/archiv_dwd_dt.html (accessed on 13 October 2023)), with the red square corresponding to the CEZ location.

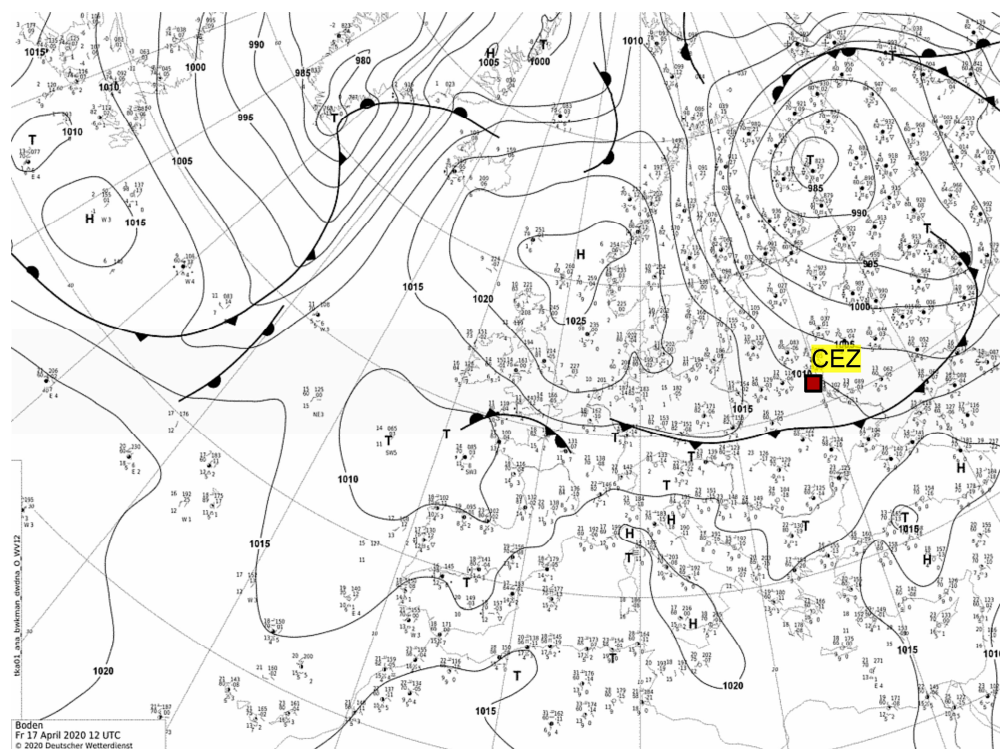


Figure A4. DWD archive synoptic map at 12 UTC on 17 April 2020 (source https://www.wetter3.de/archiv_dwd_dt.html (accessed on 13 October 2023)), with the red square corresponding to the CEZ location.

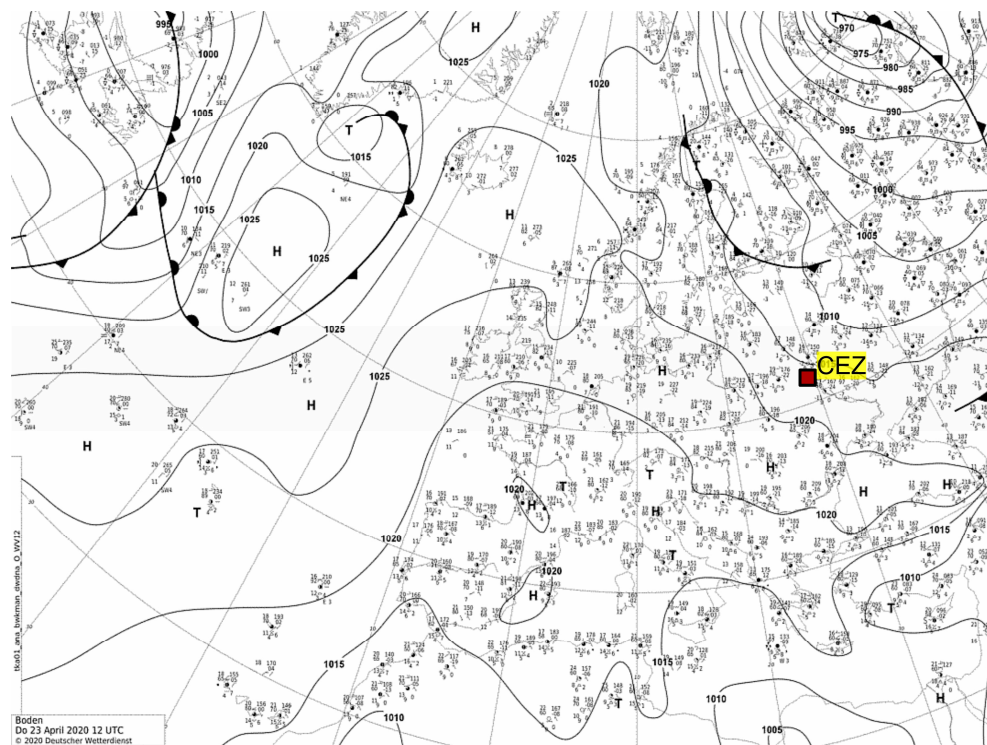


Figure A5. DWD archive synoptic map at 12 UTC on 23 April 2020 (source https://www.wetter3.de/archiv_dwd_dt.html (accessed on 13 October 2023)), with the red square corresponding to the CEZ location.

Appendix B

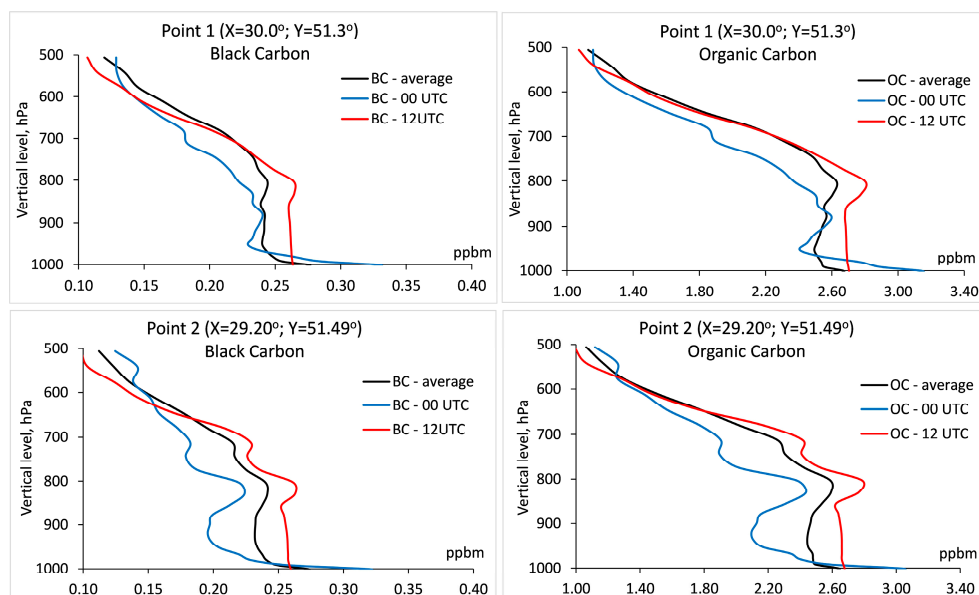


Figure A6. Vertical profiles of average, nighttime (00 UTC), and daytime (12 UTC) concentrations of BC and OC over two points with intense wildfires (the x-axes for BC and OC are different for better visibility). Point 1 refers to the CEZ; point 2 refers to the wildfires at the border of the Zhytomyr and Kyiv regions.

Appendix C

Table A1. Statistical metrics (errors) of the Enviro-HIRLAM model runs in comparison to the observed values.

Error	15 km				5 km				2 km			
	REF	DAE	IDAE	COMB	REF	DAE	IDAE	COMB	REF	DAE	IDAE	COMB
2 m air temperature (°C)												
ME	−0.11	−1.02	−0.15	<u>−1.06</u>	0.07	0.09	−0.83	0.07	−0.04	−0.11	−0.09	−0.13
MAE	1.22	2.02	1.22	<u>2.05</u>	1.24	1.38	1.94	1.37	1.28	1.34	1.27	1.34
RMSE	1.56	2.62	1.56	<u>2.68</u>	1.62	1.89	3.61	1.87	1.64	1.76	1.62	1.75
MAPE	0.36	0.47	0.36	0.47	0.51	<u>0.54</u>	<u>0.54</u>	<u>0.54</u>	0.41	0.43	0.41	0.43
2 m relative humidity (%)												
ME	1.43	<u>2.81</u>	1.42	<u>2.81</u>	0.66	−0.06	0.79	−0.08	−0.62	−1.33	−0.63	−1.41
MAE	7.39	8.94	7.38	<u>9.02</u>	7.39	7.68	7.36	7.66	7.38	7.72	7.35	7.80
RMSE	9.57	11.39	9.52	<u>11.46</u>	9.65	10.37	9.64	10.29	9.87	10.43	9.81	10.56
MAPE	0.19	<u>0.24</u>	0.19	<u>0.24</u>	0.19	0.19	0.19	0.19	0.17	0.18	0.17	0.18
10 m wind speed (m/s)												
ME	0.39	0.12	0.38	0.10	0.39	0.41	0.37	0.40	0.27	<u>0.43</u>	0.42	0.28
MAE	1.32	1.49	1.33	<u>1.51</u>	1.36	1.40	1.35	1.40	1.46	1.42	1.33	1.30
RMSE	1.74	1.94	1.74	<u>1.97</u>	1.79	1.84	1.76	1.84	1.90	1.83	1.74	1.67
MAPE	0.47	0.49	0.47	0.49	0.47	0.48	0.47	0.48	<u>0.53</u>	0.52	0.50	0.46
total cloud cover (fraction)												
ME	−0.20	−0.24	−0.20	−0.23	−0.25	−0.27	−0.23	−0.27	−0.31	<u>−0.32</u>	−0.31	<u>−0.32</u>
MAE	0.25	0.29	0.26	0.29	0.29	0.30	0.28	0.30	0.33	<u>0.34</u>	0.33	<u>0.34</u>
RMSE	0.37	0.42	0.38	0.41	0.42	0.44	0.41	0.43	0.46	<u>0.48</u>	<u>0.48</u>	<u>0.48</u>
MAPE	nd	nd	nd	nd	nd	nd	nd	nd	nd	nd	nd	nd
6 h total precipitation (mm)												
ME	0.32	0.22	0.25	0.23	<u>0.34</u>	0.25	0.33	0.18	0.20	0.12	0.16	−0.03
MAE	0.62	0.69	0.65	<u>0.77</u>	0.59	0.71	0.63	0.69	0.63	0.70	0.58	0.68
RMSE	1.32	1.54	1.34	<u>1.82</u>	1.30	1.74	1.44	1.75	1.52	1.69	1.48	1.71
MAPE	nd	nd	nd	nd	nd	nd	nd	nd	nd	nd	nd	nd

XX: the lowest error among model runs; XX: the largest error among model runs; nd: not defined.

References

- Viana, M.; Pey, J.; Querol, X.; Alastuey, A.; de Leeuw, F.; Lükewille, L. Natural sources of atmospheric aerosols influencing air quality across Europe. *Sci. Total Environ.* **2014**, *472*, 825–833. [[CrossRef](#)] [[PubMed](#)]
- Jiang, Y.; Yang, X.-Q.; Liu, X.; Qian, Y.; Zhang, K.; Wang, M.; Li, F.; Wang, Y.; Lu, Z. Impacts of Wildfire Aerosols on Global Energy Budget and Climate: The Role of Climate Feedbacks. *J. Clim.* **2020**, *33*, 3351–3366. [[CrossRef](#)]
- Liu, Y.; Stanturf, J.; Goodrick, S. Trends in global wildfire potential in a changing climate. *For. Ecol. Manag.* **2010**, *259*, 685–697. [[CrossRef](#)]
- Senande-Rivera, M.; Insua-Costa, D.; Miguez-Macho, G. Spatial and temporal expansion of global wildland fire activity in response to climate change. *Nat. Commun.* **2022**, *13*, 1208. [[CrossRef](#)] [[PubMed](#)]
- Soshenskyi, O.; Zibtsev, S.; Gumeniuk, V.; Goldammer, J.G.; Vasylyshyn, R.; Blyshchyk, V. The current landscape fire management in Ukraine and strategy for its improvement. *Environ. Socio-Econ. Stud.* **2021**, *9*, 39–51. [[CrossRef](#)]
- Savenets, M.; Osadchyi, V.; Komisar, K.; Zhemera, N.; Oreshchenko, A. Remotely visible impacts on air quality after a year-round full-scale Russian invasion of Ukraine. *Atmos. Pollut. Res.* **2023**, *14*, 101912. [[CrossRef](#)]
- Zibtsev, S.; Soshenskyi, O.; Melnykovych, M.; Blaser, J.; Waeber, P.O.; Garcia, C. Ukrainian forests in the focus of climate crisis, war and fire disasters. *Schweiz. Z. Forstwes.* **2023**, *174*, 115–117. [[CrossRef](#)]
- Savenets, M.; Osadchyi, V.; Oreshchenko, A.; Pysarenko, L. Air Quality Changes in Ukraine during the April 2020 Wildfire Event. *Geogr. Pannonica.* **2020**, *24*, 271–284. [[CrossRef](#)]

9. Kovalets, I.V.; Talerko, M.; Synkevych, R.; Koval, S. Estimation of Cs-137 emissions during wildfires and dust storm in Chernobyl Exclusion Zone in April 2020 using ensemble iterative source inversion method. *Atmos. Environ.* **2022**, *288*, 119305. [[CrossRef](#)]
10. Masson, O.; Romanenko, O.; Saunier, O.; Kirieiev, S.; Protsak, V.; Laptev, G.; Voitsekhovych, O.; Durand, V.; Coppin, F.; Steinhauser, G.; et al. Europe-Wide Atmospheric Radionuclide Dispersion by Unprecedented Wildfires in the Chernobyl Exclusion Zone, April 2020. *Environ. Sci. Tech.* **2021**, *55*, 13834–13848. [[CrossRef](#)] [[PubMed](#)]
11. Senf, F.; Heinold, B.; Kubin, A.; Müller, J.; Schrödner, R.; Tegen, I. How the extreme 2019–2020 Australian wildfires affected global circulation and adjustments. *Atmos. Chem. Phys.* **2023**, *23*, 8939–8958. [[CrossRef](#)]
12. Tosca, M.G.; Randerson, J.T.; Zender, C.S. Global impact of smoke aerosols from landscape fires on climate and the Hadley circulation. *Atmos. Chem. Phys.* **2013**, *13*, 5227–5241. [[CrossRef](#)]
13. Baró, R.; Palacios-Peña, L.; Baklanov, A.; Balzarini, A.; Brunner, D.; Forkel, R.; Hirtl, M.; Honzak, L.; Pérez, J.L.; Pirovano, G.; et al. Regional effects of atmospheric aerosols on temperature: An evaluation of an ensemble of online coupled models. *Atmos. Chem. Phys.* **2017**, *17*, 9677–9696. [[CrossRef](#)]
14. Chen, J.; Chen, I.; Tsai, I. Dynamic Feedback of Aerosol Effects on the East Asian Summer Monsoon. *J. Clim.* **2016**, *29*, 6137–6149. [[CrossRef](#)]
15. Hodnebrog, Ø.; Myhre, G.; Forster, P.; Sillmann, J.; Samset, B.H. Local biomass burning is a dominant cause of the observed precipitation reduction in southern Africa. *Nat. Commun.* **2016**, *7*, 11236. [[CrossRef](#)] [[PubMed](#)]
16. Rap, A.; Scott, C.E.; Spracklen, D.V.; Bellouin, N.; Forster, P.M.; Carslaw, K.S.; Schmidt, A.; Mann, G. Natural aerosol direct and indirect radiative effects. *Geophys. Res. Lett.* **2013**, *40*, 3297–3301. [[CrossRef](#)]
17. Makar, P.A.; Akingunola, A.; Chen, J.; Pabla, B.; Gong, W.; Stroud, C.; Sioris, C.; Anderson, K.; Cheung, P.; Zhang, J.; et al. Forest-fire aerosol–weather feedbacks over western North America using a high-resolution, online coupled air-quality model. *Atmos. Chem. Phys.* **2021**, *21*, 10557–10587. [[CrossRef](#)]
18. Bernstein, D.N.; Hamilton, D.S.; Krasnoff, R.; Mahowald, N.M.; Connelly, D.S.; Tilmes, S.; Hess, P.G.M. Short-term impacts of 2017 western North American wildfires on meteorology, the atmosphere’s energy budget, and premature mortality. *Environ. Res. Lett.* **2021**, *16*, 064065. [[CrossRef](#)]
19. Chang, D.Y.; Yoon, J.; Lelieveld, J.; Park, S.K.; Yum, S.S.; Kim, J.; Jeong, S. Direct radiative forcing of biomass burning aerosols from the extensive Australian wildfires in 2019–2020. *Environ. Res. Lett.* **2021**, *16*, 044041. [[CrossRef](#)]
20. Xu, L.; Zhu, Q.; Riley, W.J.; Chen, Y.; Wang, H.; Ma, P.; Randerson, J.T. The Influence of Fire Aerosols on Surface Climate and Gross Primary Production in the Energy Exascale Earth System Model (E3SM). *J. Clim.* **2021**, *34*, 7219–7238. [[CrossRef](#)]
21. Yu, H.; Liu, S.C.; Dickinson, R.E. Radiative effects of aerosols on the evolution of the atmospheric boundary layer. *Atmospheres* **2002**, *107*, D12. [[CrossRef](#)]
22. Iltoviz, E.; Khain, A.P.; Benmoshe, N.; Phillips, V.T.J.; Ryzhkov, A.V. Effect of Aerosols on Freezing Drops, Hail, and Precipitation in a Midlatitude Storm. *J. Atmos. Sci.* **2016**, *73*, 109–144. [[CrossRef](#)]
23. Zhang, Y.; Fan, J.; Shrivastava, M.; Homeyer, C.R.; Wang, Y.; Seinfeld, J.H. Notable impact of wildfires in the western United States on weather hazards in the central United States. *PNAS* **2022**, *119*, e2207329119. [[CrossRef](#)] [[PubMed](#)]
24. Ackerman, A.S.; Toon, O.B.; Stevens, D.E.; Heymsfield, A.J.; Ramanathan, V.; Welton, E.J. Reduction of tropical cloudiness by soot. *Science* **2000**, *288*, 1042–1047. [[CrossRef](#)]
25. Grell, G.; Freitas, S.R.; Stuefer, M.; Fast, J. Inclusion of biomass burning in WRF-Chem: Impact of wildfires on weather forecasts. *Atmos. Chem. Phys.* **2011**, *11*, 5289–5303. [[CrossRef](#)]
26. Zhang, Y.; Fu, R.; Yu, H.; Qian, Y.; Dickinson, R.; Assunção, M.; Silva Dias, F.; da Silva Dias, P.L.; Fernandes, K. Impact of biomass burning aerosol on the monsoon circulation transition over Amazonia. *Geophys. Res. Lett.* **2009**, *36*, L10814. [[CrossRef](#)]
27. Fan, J.; Wang, Y.; Rosenfeld, D.; Liu, X. Review of Aerosol–Cloud Interactions: Mechanisms, Significance, and Challenges. *J. Atmos. Sci.* **2016**, *73*, 4221–4252. [[CrossRef](#)]
28. Da Silva, N.; Mailler, S.; Drobinski, P. Aerosol indirect effects on summer precipitation in a regional climate model for the Euro-Mediterranean region. *Ann. Geophys.* **2018**, *36*, 321–335. [[CrossRef](#)]
29. White, B.; Gryspeerdt, E.; Stier, P.; Morrison, H.; Thompson, G.; Kipling, Z. Uncertainty from the choice of microphysics scheme in convection-permitting models significantly exceeds aerosol effects. *Atmos. Chem. Phys.* **2017**, *17*, 12145–12175. [[CrossRef](#)]
30. Baklanov, A.; Smith Korsholm, U.; Nuterman, R.; Mahura, A.; Nielsen, K.P.; Sass, B.H.; Rasmussen, A.; Zakey, A.; Kaas, E.; Kurganskiy, A.; et al. Enviro-HIRLAM online integrated meteorology–chemistry modelling system: Strategy, methodology, developments and applications (v7.2). *Geosci. Model Dev.* **2017**, *10*, 2971–2999. [[CrossRef](#)]
31. Savenets, M.; Pysarenko, L.; Krakovska, S.; Mahura, A.; Petäjä, T. Enviro-HIRLAM model estimates of elevated black carbon pollution over Ukraine resulted from forest fires. *Atmos. Chem. Phys.* **2022**, *22*, 15777–15791. [[CrossRef](#)]
32. Jolliffe, I.T.; Stephenson, D.B. *Forecast Verification: A Practitioner’s Guide in Atmospheric Science*; Wiley: Hoboken, NJ, USA, 2003.
33. Tuccella, P.; Menut, L.; Briant, R.; Deroubaix, A.; Khvorostyanov, D.; Mailler, S.; Siour, G.; Turquety, S. Implementation of Aerosol–Cloud Interaction within WRF-CHIMERE Online Coupled Model: Evaluation and Investigation of the Indirect Radiative Effect from Anthropogenic Emission Reduction on the Benelux Union. *Atmosphere* **2019**, *10*, 20. [[CrossRef](#)]

34. Jung, J.; Souri, A.H.; Wong, D.C.; Lee, S.; Jeon, W.; Kim, J.; Choi, Y. The impact of the direct effect of aerosols on meteorology and air quality using aerosol optical depth assimilation during the KORUS-AQ campaign. *J. Geophys. Res. Atmos.* **2019**, *124*, 8303–8319. [[CrossRef](#)] [[PubMed](#)]
35. Carter, T.S.; Heald, C.L.; Jimenez, J.L.; Campuzano-Jost, P.; Kondo, Y.; Moteki, N.; Schwarz, J.P.; Wiedinmyer, C.; Darmenov, A.S.; da Silva, A.M.; et al. How emissions uncertainty influences the distribution and radiative impacts of smoke from fires in North America. *Atmos. Chem. Phys.* **2020**, *20*, 2073–2097. [[CrossRef](#)]

Disclaimer/Publisher’s Note: The statements, opinions and data contained in all publications are solely those of the individual author(s) and contributor(s) and not of MDPI and/or the editor(s). MDPI and/or the editor(s) disclaim responsibility for any injury to people or property resulting from any ideas, methods, instructions or products referred to in the content.